Summer 2014

Gaussian beam scattering from a deterministic rough metal surface

Qi Wang
New Jersey Institute of Technology

ABSTRACT

GAUSSIAN BEAM SCATTERING FROM A DETERMINISTIC ROUGH METAL SURFACE

by
Qi Wang

A full-wave theory of plane wave scattering from rough surfaces called the Correction Current (CC) method was recently developed for the two-dimensional scatter problem that have a one-dimensional roughness profile. The method involves a primary field and radiation modes that are plane-wave-type fields that satisfy the boundary conditions at the rough surface. These fields do not satisfy Maxwell's source free equations, but they are forced to satisfy Maxwell's equations with distributed sources upon the introduction of fictitious volume currents distributions which correct for the field errors. Additionally, current sheet distributions are introduced which generate a radiation modal field that satisfies the boundary conditions, the radiation condition for plane waves, and Maxwell's equations with distributed sources. The scatter problem is solved by eliminating these volume and sheet current densities in an iterative procedure which produces a composite field that satisfies all requirements. Reciprocity is satisfied by using only the first-order field solution. The first-order solution of the CC method reduces to the small perturbation and the Kirchhoff methods in the regions of validity and is more accurate than these methods in regions where neither are considered valid. This paper extends the CC method to the more general and important case of beam wave scattering by a deterministic rough metal surface.

GAUSSIAN BEAM SCATTERING FROM A DETERMINISTIC ROUGH METAL SURFACE

by
Qi Wang

A Thesis
Submitted to the Faculty of
New Jersey Institute of Technology
in Partial Fulfillment of the Requirements for the Degree of
Master of Science in Electrical Engineering

Department of Electrical and Computer Engineering

August 2014

APPROVAL PAGE

GAUSSIAN BEAM SCATTERING FROM A DETERMINISTIC ROUGH METAL SURFACE

Qi Wang

Dr. Gerald M. Whitman, Thesis Advisor Professor of Electrical and Computer Engineering, NJIT	Date
Dr. Marek Sosnowski, Committee Member Professor of Electrical and Computer Engineering, NJIT	Date
Dr. Haim Grebel, Committee Member Professor of Electrical and Computer Engineering, NJIT	Date

BIOGRAPHICAL SKETCH

Author: Qi Wang

Degree: Master of Science

Date: August 2014

Undergraduate and Graduate Education:

- Master of Science in Electrical Engineering,
  New Jersey Institute of Technology, Newark, NJ, 2014

- Bachelor of Science in Electrical Engineering,
  Xidian University, Xi'an, Shaanxi, P. R. China, 2012

Major: Electrical Engineering

To my beloved family

爸爸妈妈我永远爱你们！

ACKNOWLEDGMENT

I would like to express my sincere appreciation to Professor Gerald Whitman for his teaching, guidance and patience during the two years. Every semester I took one of his classes. He is the one professor who has witnessed my professional and personal growth in the USA for the last two years. What I have learned from him is not only the materials of his courses or for this thesis, but also how to live and communicate in a foreign country. He has encouraged me a lot. Special thanks are given to students: Anthony Triolo, Byung-Tae Yoon, Paul Spector for their prior work on this research. I wish also to thank Dr. Marek Sosnowski, Dr. Haim Grebel for their participation as members of my thesis committee.

I especially want to thank my parents, Bao-gui Wang and Xiao-li Huang for their continuous support and encouragement.

TABLE OF CONTENTS

LIST OF FIGURES

CHAPTER 1

INTRODUCTION

Since all real surfaces are rough, there is considerable interest among researchers to understand how rough surfaces affect the scattering of incident waves. Advancement in this area of research is useful in many fields, such as cellular communication, optics, radar targeting and detection, medical imaging, antenna design, and radio astronomy. Scattering plays an important role in situations involving high frequency waves, where the size of surface perturbations is a certain fraction of the wavelength of the incident wave. Scattering depends not only on the relationship between wavelength and surface variations, but also on the angle of incidence, the polarization of the incident wave, and the electric properties of the surface. In scattering experiments, the incident field is a beam wave that is excited by an antenna or a laser. Theoretical studies of scattering, however, often assume an incident plane wave to simplify the analysis. This was done in [1-2] in the development of the full wave solution called the Correction Current (CC) method for plane wave scattering from rough metal and dielectric surfaces[1]. The CC method as developed for plane wave rough surface scattering in [1] was shown to provide a first-order solution that satisfies reciprocity and bridges the gap between the small perturbation and Kirchhoff theories, to furnish error criteria to determine its range of validity, and to be mathematically rigorous and physically clear. Refer to [1] for comparisons and references concerning several other methods for rough surface scattering, such as the Rayleigh or small-perturbation method, the Kirchhoff or physical optics approximation, the full-wave

[1] In [1], the CC theory was applied to deterministic rough surface with a well defined roughness profile as well as to random rough surfaces that have Gaussian statistics such that end effects due to the finite width of the rough surface corrugations are negligible.

solutions of Bahar and Thorsos's method of moment/integral equation approach. In this dissertation, the CC method is extended to beam wave scattering from a deterministic rough metal surface.

Chapter 2 reviews Gaussian beams and their properties. The full wave theory for rough surface scattering, known as the Correction Current (CC) method, is then developed for scattering of an incident Gaussian beam from a perfectly conducting infinite plate with finite rough surface segment (PEC). The scatter geometry is two dimensional and the scatter profile depends on one variable. The electric field of the incident beam wave is derived for the two dimension coordinate system (x, z). The first-order scatter pattern formula is derived from knowledge of the scatter pattern formula for an incident plane wave since the beam wave is represented by a superposition of plane waves. A conservation of power criterion is presented and an approximate formula for the CC beam wave scatter pattern is also derived.

Chapter 3 reviews the well-known numerical method used to solve a variety of electromagnetic problems called the Method of Moment (MOM). This numerical method is used as the reference solution for comparison to the CC method. The MOM solution is developed for scattering from the perfectly conducting plate with a finite rough surface segment using image theory. The numerical procedure is illustrated for scattering from a single bump on an infinite planar perfect conductor.

Chapter 4 presents the definition of the normalized power scatter pattern and numerical results using the CC method and the Method of Moments.

Finally, conclusions and possible extensions are discussed in Chapter 5.

CHAPTER 2

FORMULATION AND SOLUTION OF BEAM WAVE SCATTER PROBLEM BY USE OF THE CC METHOD

The scatter problem under consideration is shown in Figure 2.1. The geometry and all the field quantities are two dimensional and are independent of the y-coordinate variable. The reference two-dimensional coordinate system is (x,z). A perfectly conducting metal surface lies along the z-axis that has a one-dimensional sinusoidal roughness profile $D(\mathrm{z}) = D_0\left[1-\sin^2\left(\frac{N_b}{2}\pi\frac{z}{L}\right)\right]$ in the region $|z| \le L$, but is planar ($D=0$) over the region $|z| \ge L$, where N_b is the number of bumps. Above the metal surface is air. At $z=\pm L$, the surface height $D(\mathrm{z})$ and the surface slope $D' = dD/dz$ are continuous.

The aperture antenna shown in the Figure 2.1 is the source of the incident beam radiation. The antenna's main beam axis points toward the origin of the (x,z) coordinate system in the direction φ_0 measured positive from the positive x-axis. The origin of the primed coordinates (x',z') is located in the antenna's aperture plane $x'=0$ at the phase center of the antenna at the point (x_0,z_0), a distance ρ_0 from the origin of the reference coordinate system (x,z). From the geometry of Figure 2.1, $x_0 = \rho_0\cos\varphi_0 > 0$ and $z_0 = -\rho_0\sin\varphi_0 < 0$.

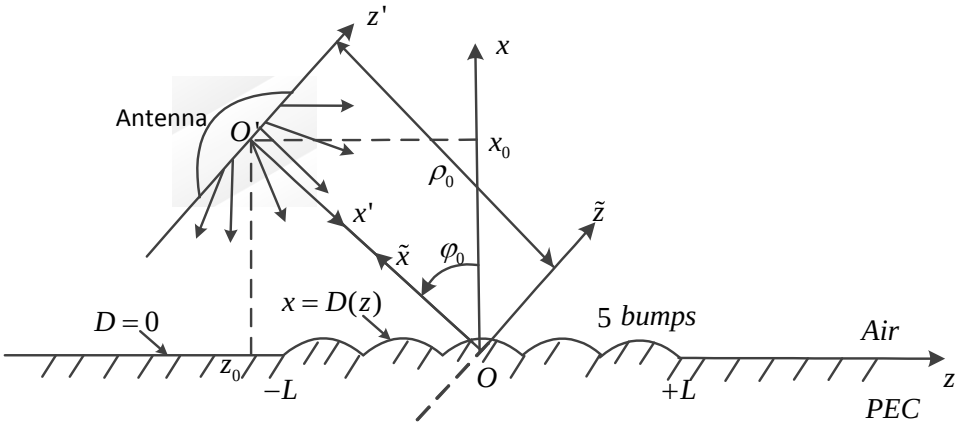

Figure 2.1 Rough PEC surface illuminated by a Gaussian beam due to an aperture antenna. Rays eminating from the antenna represent the spectrum of plane waves of the beam.

2.1 Incident Plane Wave

Before expressions for the incident Gaussian Beam are introduced, it is convenient to first describe an incident plane wave. This is needed because the Gaussian beam is expressed as a superposition or angular spectrum of plane waves.

Consider the TE polarized incident plane wave in air that propagates in the wave vector direction $\boldsymbol{k}^i$ at an angle α measured positive from the positive x'-axis as shown in Figure 2.2. This plane wave is written as

$$\boldsymbol{E}^{i,PL} = \hat{\boldsymbol{y}} E_y^{i,PL}\left(x', z'\right) = \hat{\boldsymbol{y}} E_0{}^i e^{-j\boldsymbol{k}^i \cdot \boldsymbol{r}}, \tag{2.1}$$

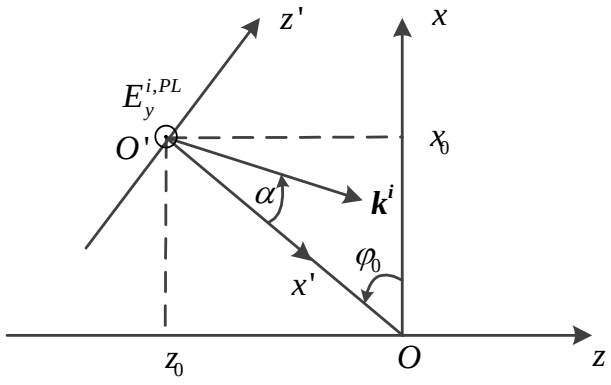

Figure 2.2 Plane wave in direction $\boldsymbol{k}^i$.

where the incident wave vector and the position vector measured from the antenna's phase center are given by, respectively,

$$\boldsymbol{k}^{i} = k_{x'}\hat{\boldsymbol{x}}' + k_{z'}\hat{\boldsymbol{z}}', \ \boldsymbol{r} = x'\hat{\boldsymbol{x}}' + z'\hat{\boldsymbol{z}}', \tag{2.1a}$$

with wave vector components

$$k_{x'} = k_0 \cos\alpha \tag{2.1b}$$

$$k_{z'} = k_0 \sin\alpha . \tag{2.1c}$$

Substituting (2.1b) and (2.1c) into (2.1) gives

$$E_y^{i,PL}(x', z') = E_0^{\,i} e^{-jk_0[x'\cos\alpha + z'\sin\alpha]}. \tag{2.2}$$

The incident plane wave formula (2.2) needs to be expressed in terms of the reference coordinates (x, z). To do this, it is convenient to first introduce the rotated coordinates $(\tilde{x}, \tilde{z})$, which are defined in Figure 2.3 and given by the coordinate transformations $x' = \rho_0 - \tilde{x}$, $z' = \tilde{z}$. Substituting these transformations into equation (2.2) gives

$$E_y^{i,PL}(\tilde{x}, \tilde{z}) = E_0^{\,i} e^{-jk_0\left[(\rho_0 - \tilde{x})\cos\alpha + \tilde{z}\sin\alpha\right]} \tag{2.3}$$

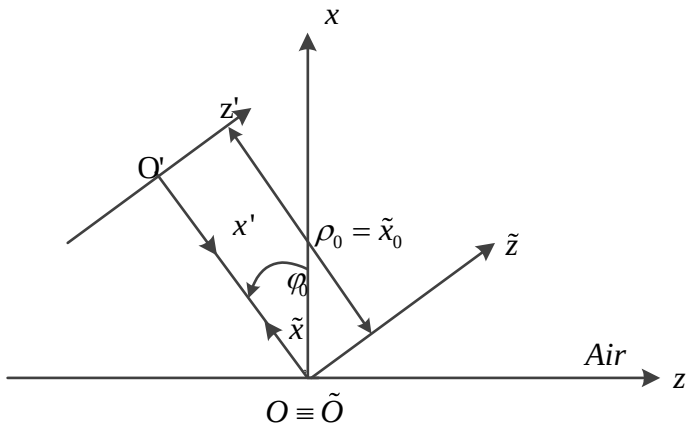

Figure 2.3 Coordinate systems (x, z), $(\tilde{x}, \tilde{z})$ and (x', z').

As shown in Figure 2.3, the $(\tilde{x},\tilde{z})$ coordinates are related to the (x,z) coordinates via the coordinate transformations

$$\begin{aligned}\tilde{x} &= x\cos\varphi_0 - z\sin\varphi_0 \\ \tilde{z} &= x\sin\varphi_0 + z\cos\varphi_0\end{aligned} \tag{2.4}$$

Substituting (2.4) into (2.3) gives, after using trigonometry,

$$E_y^{i,PL}(x,z) = E_0{}^i e^{-jk_0\rho_0\cos\alpha} e^{jk_0 x\cos(\alpha+\varphi_0)} e^{-jk_0 z\sin(\alpha+\varphi_0)}. \tag{2.5}$$

Equation (2.5) is a TE polarized electric field plane wave that propagates in the angular direction α measured positive from the positive x'-axis or, equivalently, propagates in the angular direction $(\alpha+\varphi_0)$ measured positive from the positive x-axis. This incident plane wave field has an amplitude $E_0{}^i e^{-jk_0\rho_0\cos\alpha}$ at the origin of the (x,z) coordinate system.

2.2 Incident Gaussian Beam

2.2.1 Gaussian Beam

In optics, a Gaussian beam is a beam of electromagnetic radiation whose transverse electric field and intensity distributions are well approximated by Gaussian functions. In this section, it will be assumed that a Gaussian beam propagates in the z direction in the cylindrical coordinate system (ρ,φ,z) [2] so that it is rotationally symmetry and, therefore, independent of the polar angle φ. A mathematical expression for the complex electric field amplitude of a Gaussian beam is [3]

$$E(\rho,z) = E_0\frac{w_0}{w(z)}exp\left(\frac{-\rho^2}{w(z)^2} - ikz - ik\frac{\rho^2}{2R(z)} + i\zeta(z)\right) \tag{2.6}$$

[2] The symbolic notation for coordinate and parameters used in this section is not consistent with Section 2.1.

where

$$w(\mathrm{z}) = w_0\left[1+\left(\frac{z}{z_1}\right)^2\right]^{1/2}, \tag{2.6a}$$

$$R(\mathrm{z}) = z\left[1+\left(\frac{z_1}{z}\right)^2\right], \tag{2.6b}$$

$$\zeta(\mathrm{z}) = \tan^{-1}\frac{z}{z_1}, \tag{2.6c}$$

$$w_0 = w(0) = \left(\frac{\lambda z_1}{\pi}\right)^{1/2}. \tag{2.6d}$$

ρ is the radial distance from the center axis of the beam; z is the axial distance from the beam's narrowest point (the "waist"); $k = 2\pi/\lambda$ is the wave number (in radians per meter); $E_0 = |E(0,0)|$; z_1 is known as the Rayleigh range; $w(\mathrm{z})$ is the measure of the beam width; w_0 is the beam waist; $R(\mathrm{z})$ is the radius of curvature of the beam's wavefronts, and $\zeta(\mathrm{z})$ is the Gouy phase shift.

The optical intensity $I(\rho, z) = |E(\rho, z)|^2$ is a function of the axial and radial distance z and $\rho = (x^2 + y^2)^{1/2}$. For the Gaussian beam (2.6), intensity is given by

$$I(\rho, z) = I_0\left[\frac{w_0}{w(\mathrm{z})}\right]^2 exp\left[-\frac{2\rho^2}{w^2(\mathrm{z})}\right] \tag{2.7}$$

where $I_0 = |E_0|^2$. At each value of z, the intensity is a Gaussian function of the radial distance ρ. This is why the wave is called a Gaussian beam. The Gaussian function has its peak at $\rho = 0$ (on the z-axis) and drops monotonically with increasing ρ. The width $w(\mathrm{z})$ of the Gaussian distribution increases with the axial distance z.

The total optical power P carried by the beam is the integral of the optical intensity over a transverse plane at a specified distance z. Thus,

$$P = \int_0^{\infty} I(\rho, z) 2\pi\rho d\rho , \tag{2.8}$$

which reduces to

$$P = \frac{1}{2} I_0 (\pi w_0^{\,2}) . \tag{2.8a}$$

This result is independent of z as expected since the medium is lossless. The ratio of the power carried within a circle of radius ρ_1 in the transverse plane at position z to the total power is

$$\frac{1}{P} \int_0^{\rho_1} I(\rho, z) 2\pi\rho d\rho = 1 - exp\left[-\frac{2\rho_1^{\,2}}{w^2(z)} \right] \tag{2.9}$$

The power contained within a circle of radius $\rho_1 = w(z)$ is approximately 86% of the total power. About 99% of the power is contained within a circle of radius $1.5\, w(z)$. Since 86% of power is carried within a circle of radius $w(z)$, $w(z)$ is regarded as the beam radius (also called the beam width).

The dependence of the beam radius on z is governed by (2.6a) ,

$$w(\mathrm{z}) = w_0 \left[1 + \left(\frac{z}{z_1} \right)^2 \right]^{1/2} . \tag{2.6a}$$

The beam radius $w(z)$ reaches its minimum value w_0 in the plane $z = 0$ and is called the beam waist, w_0 is also called the waist radius. The beam radius increases gradually with z ,

reaching $\sqrt{2}w_0$ at $z = z_1$, and continues increasing monotonically with z. For $z \gg z_1$, the first term of (2.6a) may be neglected, resulting in the linear relation

$$w(z) \approx \frac{w_0}{z_1} z = \theta_0 z \text{ for } z \gg z_1, \tag{2.10}$$

where

$$\theta_0 \equiv w_0 / z_1 = \frac{2}{\pi} \frac{\lambda}{2w_0} \tag{2.10a}$$

is a cone with half-angle θ_0. About 86% of the beam power is confined within this cone. The beam divergence θ_0 is directly proportional to the ratio of wavelength λ and the beam-waist diameter $2w_0$. If the waist is squeezed, the beam diverges. To obtain a highly directional beam, a short wavelength (high frequency) and fat beam waist should be used.

2.2.2 Incident Gaussian Beam as a Spectrum of Plane Waves

The aperture antenna in Figure 2.1 is assumed to produce a tangential y-directed[3] (TE polarized) electric field that has a real Gaussian amplitude distribution[4] in the aperture plane $x' = 0$ at the antenna phase center as shown in Figure 2.4, which is given by

$$E_y^{i,B}(x' = 0, z') = E_0 e^{-(z'/w_0)^2}. \tag{2.11}$$

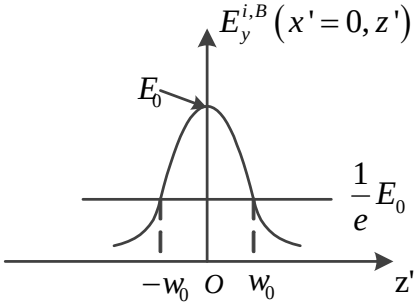

Figure 2.4 Gaussian amplitude distribution in the antenna aperture plane $x' = 0$.

[3] The symbolic notation for coordinate and parameters used in this section and those to follow is consistent with Section 2.1.
[4] The Gaussian amplitude distribution is real because the antenna phase centre is located in the aperture plane.

The antenna aperture diameter $2w_0$ is chosen such that the aperture illumination is negligible at the aperture edges. Thus, the antenna aperture can be taken to be infinite in extent for the determination of the field radiated by the antenna [4]. To extend the CC method, which was developed for plane wave scattering from a rough metal surface, to beam wave scattering, a representation of the incident Gaussian beam as a superposition of plane waves is needed. Such a representation at an arbitrary point (x', z') in free space (air) is given by the inverse Fourier transform

$$E_y^{i,B}(x', z') = \int_{-\infty}^{+\infty} [E(k_{z'}) e^{-jk_{x'}x' - jk_{z'}z'}] dk_{z'}, \tag{2.12}$$

where $E(k_{z'})$ are the amplitudes of the plane wave spectral components. The spectrum of plane waves in (2.12) contain both propagating and evanescent plane waves since $k_{x'} = \sqrt{k_0^{\,2} - k_{z'}^{\,2}}$ is real for $k_0^{\,2} > k_{z'}^{\,2}$ and negative imaginary for $k_0^{\,2} < k_{z'}^{\,2}$, where k_0 is the free space wavenumber. Each plane wave constituent has a wave vector direction given by $\boldsymbol{k} = k_{x'}\hat{\boldsymbol{x}}' + k_{z'}\hat{\boldsymbol{z}}'$ and may be associated with a real angular direction of propagation α in the range $-\pi/2 \le \alpha \le \pi/2$ as can be seen from Figure 2.2.

Since $$E_y^{i,B}(x' = 0, z') = \int_{-\infty}^{+\infty} [E(k_{z'}) e^{-jk_{z'}z'}] dk_{z'} = E_0 e^{-(z'/w_0)^2} \tag{2.13}$$

is the inverse Fourier transform of $E(k_{z'})$, the spectral amplitude $E(k_{z'})$ can be obtained from the Fourier transform,

$$E(k_{z'}) = \frac{1}{2\pi} \int_{-\infty}^{+\infty} E_y^{\,i}(x' = 0, z') e^{+jk_{z'}z'}] dk_{z'} = \frac{E_0 w_0}{2\sqrt{\pi}} e^{(-k_{z'}w_0)^2/4}. \tag{2.14}$$

Substituting (2.14) into (2.12) gives

$$E_y^{i,B}(x',z') = \frac{E_0 w_0}{2\sqrt{\pi}} \int_{-\infty}^{+\infty} e^{-(k_{z'} w_0/2)^2} e^{-jk_{x'}x' - jk_{z'}z'} dk_{z'} \tag{2.15}$$

Expressing the incident beam wave field in (2.15) in terms of $(\tilde{x},\tilde{z})$ coordinates in Figure 2.3 using $x' = \rho_0 - \tilde{x}$ and $z' = \tilde{z}$ gives

$$E_y^{i,B}(\tilde{x},\tilde{z}) = \frac{E_0 w_0}{2\sqrt{\pi}} \int_{-\infty}^{+\infty} e^{-(k_{z'} w_0/2)^2} e^{+jk_{x'}(\tilde{x}-\rho_0)} e^{-jk_{z'}\tilde{z}} dk_{z'} \tag{2.16}$$

where ρ_0 is the distance to the antenna phase center from the origin of the $(\tilde{x},\tilde{z})$ or (x,z) coordinate system. Recall from equation (2.4) that the coordinates $(\tilde{x},\tilde{z})$ are related to the coordinates (x,z) by rotation through the angle φ_0.

The spectrum of plane waves of the incident beam in (2.16) includes propagating and evanescent plane waves. For ρ_0 sufficiently large, evanescent waves in (2.16) do not reach the scatter surface and are neglected. In addition, plane waves that do not travel toward the scatter surface are excluded. Hence, as can be seen from Figure 2.5, the allowable angular plane wave directions α associated with the incident beam wave fall in the range $-\pi/2 \le \alpha \le \alpha_0^+$, where $\alpha_0^+ = \pi/2 - \varphi_0$. The angular direction α_0^+ is associated with the direction of the plane wave that travels in the +z direction parallel to the $x = 0$ plane and constitutes the upper bound for incident waves that can strike the scatter surface; plane waves in the range $\alpha_0^+ < \alpha \le \pi/2$ cannot strike the metal scatterer.

Assuming that the incident beam is symmetric further restricts the plane wave spectrum in (2.16) to angular directions α that fall in the truncated range $-\alpha_0^+ \le \alpha \le \alpha_0^+$. This range of directional angles α corresponds to values of $k_{z'}$ in the range

$-k_0 \cos\varphi_0 \le k_{z'} \le k_0 \cos\varphi_0$ since $k_{z'} = k_0 \sin\alpha$. Thus, the incident Gaussian beam as originally represented by the infinite spectrum of pane waves in equation (2.16) is now represented by the truncated spectrum of plane waves given by

$$E_y^{i,B}(\tilde{x},\tilde{z}) = \frac{E_0 w_0}{2\sqrt{\pi}} \int_{-k_0\cos\varphi_0}^{+k_0\cos\varphi_0} e^{-(k_{z'}w_0/2)^2} e^{+jk_{x'}(\tilde{x}-\rho_0)} e^{-jk_{z'}\tilde{z}} dk_{z'} \tag{2.17}$$

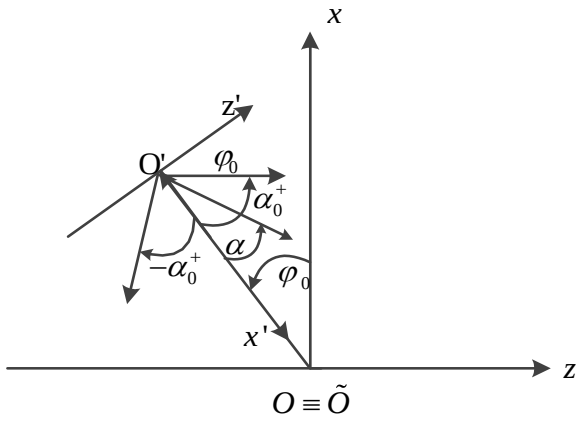

Figure 2.5 Directional angles α associated with the incident symmetric Gaussian beam.

Changing the integration variable in (2.17) from $k_{z'}$ to α using $k_{z'} = k_0 \sin\alpha$ and $k_{x'} = k_0 \cos\alpha$ yields

$$E_y^{i,B}(\tilde{x},\tilde{z}) = \frac{E_0 w_0}{2\sqrt{\pi}} \int_{-(\frac{\pi}{2}-\varphi_0)}^{+(\frac{\pi}{2}-\varphi_0)} e^{-(k_0 w_0 \sin\alpha/2)^2} e^{jk_0(\tilde{x}-\rho_0)\cos\alpha} e^{-jk_0\tilde{z}\sin\alpha} k_0 \cos\alpha d\alpha \,. \tag{2.18}$$

Defining the amplitude function

$$\mathrm{A}_0(\alpha) = \frac{\mathrm{k}_0 w_0}{2\sqrt{\pi}} \mathrm{e}^{-(\mathrm{k}_0 w_0 \sin\alpha/2)^2} \cos\alpha \tag{2.19}$$

permits re-writing (2.18) as

$$E_y^{i,B}(\tilde{x},\tilde{z}) = E_0 \int_{-(\frac{\pi}{2}-\varphi_0)}^{+(\frac{\pi}{2}-\varphi_0)} A_0(\alpha) e^{jk_0\cos\alpha(\tilde{x}-\rho_0)} e^{-jk_0\tilde{z}\sin\alpha} d\alpha . \tag{2.20}$$

Thus, the electric field of TE polarized the incident beam as represented by (2.20) is a symmetric, truncated spectrum of propagating plane waves with Gaussian amplitudes $E_0 A_0(\alpha)$. For this beam to be narrow, the Gaussian amplitude function $A_0(\alpha)$ is assumed to decay rapidly away from the main beam direction $\alpha = 0$. This means that at the end-points of the truncated α-range, $A_0(\alpha)$ is small, i.e.,

$$\frac{A_0^i(\alpha)}{A_0^i(0)} \ll 1 \text{ for } \alpha = \pm\alpha_0^+ = \pm(\frac{\pi}{2} - \varphi_0). \tag{2.21}$$

Substituting (2.19) into (2.21) gives

$$\frac{A_0(\alpha)}{A_0(0)} = e^{-\left(\frac{k_0 w_0 \sin\alpha}{2}\right)^2} \sin\varphi_0 \ll 1 \text{ for } \alpha = \pm\alpha_0^+ = \pm(\frac{\pi}{2} - \varphi_0). \tag{2.22}$$

This condition for a narrow incident beam requires φ_0 not too close to $\pi/2$ and that

$$e^{-(k_0 w_0 \cos\varphi_0/2)^2} \ll 1. \tag{2.23}$$

For reasonable φ_0 and $w_0 \geq 4$, the condition (2.23) is very well satisfied.

The incident beam field $E_y^{i,B}$ in (2.20) is now expressed in terms of (x,z) coordinates so that the first-order scatter field according to the CC method can be used. Consider (2.20) written as

$$E_y^{i,B}(\tilde{x},\tilde{z}) = E_0 \int_{-(\frac{\pi}{2}-\varphi_0)}^{+(\frac{\pi}{2}-\varphi_0)} A_0(\alpha) e^{-jk_0\rho_0\cos\alpha} \left[e^{jk_0\tilde{x}\cos\alpha - jk_0\tilde{z}\sin\alpha} \right] d\alpha . \tag{2.24}$$

Using (2.4) in (2.24) gives

$$E_y^{i,B}(x,z) = E_0 \int_{-(\frac{\pi}{2}-\varphi_0)}^{(\frac{\pi}{2}-\varphi_0)} A_0(\alpha) e^{-jk_0\rho_0\cos\alpha} e^{jk_0 x\cos(\varphi_0+\alpha)-jk_0 z\sin(\varphi_0+\alpha)} d\alpha \tag{2.25}$$

with $$A_0(\alpha) = \frac{k_0 w_0}{2\sqrt{\pi}} e^{-(k_0 w_0 \sin\alpha/2)^2} \cos\alpha\,. \tag{2.25a}$$

Combining (2.25a) and (2.25) gives

$$E_y^{i,B}(x,z) = \frac{E_0 k_0 w_0}{2\sqrt{\pi}} \int_{-(\frac{\pi}{2}-\varphi_0)}^{(\frac{\pi}{2}-\varphi_0)} e^{-(k_0 w_0 \sin\alpha/2)^2} e^{-jk_0\rho_0\cos\alpha} e^{jk_0 x\cos(\varphi_0+\alpha)-jk_0 z\sin(\varphi_0+\alpha)} \cos\alpha\, d\alpha \tag{2.26}$$

2.3 First-Order Gaussian Beam Scatter Field

It will now be shown how the CC first-order scatter field for the case of an incident plane wave is used to obtain the CC first-order scatter field for an incident beam wave.

The first-order scatter far field formula for plane wave scattering from an infinite perfectly conducting metal plate having a finite rough segment over the region $-L \le z \le +L$ using the CC method was determined and given by (28) in [1] in terms of the plane wave incident angle φ_0 and scatter angle φ; see Figure 2.6. Applying the CC scatter formula in (28) of [1] for the incident plane wave given in (2.5) requires replacing in (28) of [1] the incident angle φ_0 by the incident angle $\alpha+\varphi_0$ and the amplitude E_0 by the amplitude $E_0 e^{-jk_0\rho_0\cos\alpha}$. These substitutions yield, for the incident plane wave of (2.5), the CC first-order scatter far field formula

$$E_y^{(1),PL}\left(\rho,\varphi;\alpha+\varphi_0\right) = j\sqrt{\frac{2}{\pi}} E_0 \frac{e^{-j\left(k_0\rho+\pi/4\right)}}{\sqrt{k_0\rho}} S_{TE}^{(1),PL}\left(\varphi,\alpha+\varphi_0\right) \tag{2.26}$$

with plane wave scatter pattern

$$S_{TE}^{(1),PL}\left(\varphi,\alpha+\varphi_0\right)=\frac{k_0\cos\varphi\cos\left(\alpha+\varphi_0\right)}{\cos\varphi+\cos\left(\alpha+\varphi_0\right)}\cdot e^{-jk_0\rho_0\cos\alpha}$$
$$\cdot\int_{z_1=-L}^{L}\left[1-(1+D_1{}'^2)e^{jk_0D_1\left(\cos\varphi+\cos\left(\alpha+\varphi_0\right)\right)}\right]e^{jk_0z_1\left(\sin\varphi-\sin\left(\alpha+\varphi_0\right)\right)}dz_1 \tag{2.27}$$

for $-\frac{\pi}{2}\le\varphi\le\frac{\pi}{2}$, $-\frac{\pi}{2}\le\alpha+\varphi_0\le\frac{\pi}{2}$ and φ_0 not near $\pm\frac{\pi}{2}$,

with condition (2.23), where the observation point $\left(\rho,\varphi\right)$ lies in the far field, $x=\rho\cos\varphi$, $z=\rho\sin\varphi$ and $D_1=D\left(z_1\right)$, $D_1{}'=dD_1/dz_1$.

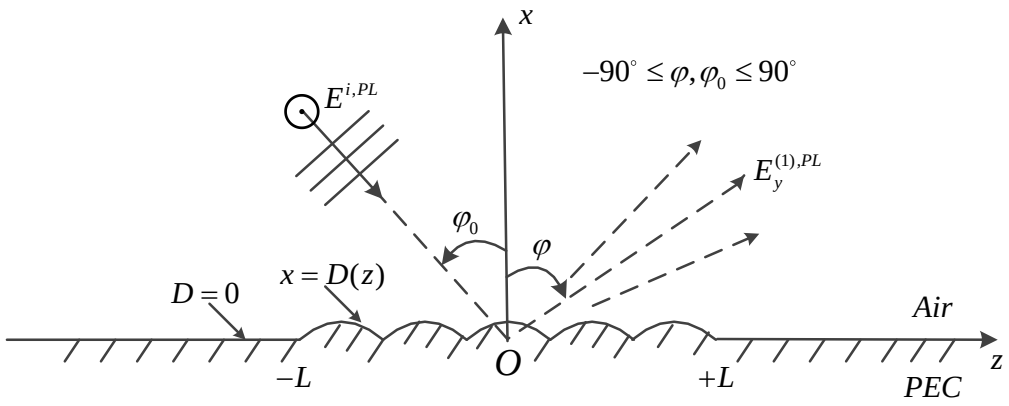

Figure 2.6 Plane wave incidence angle φ_0 and scatter angle φ of the first-order scatter field based on the CC method.

Consider now the incident Gaussian beam wave (2.25), which consists of a directional spectrum of plane waves over the finite angular domain $-(\frac{\pi}{2}-\varphi_0)\le\alpha\le(\frac{\pi}{2}-\varphi_0)$ that are incident upon the metal scatter at angles $\alpha+\varphi_0$ (measured positive from the positive x-axis) with amplitudes $E_0A_0\left(\alpha\right)$. Comparing the plane waves of the incident Gaussian beam (2.25) to the incident plane wave (2.5), which is also incident upon the metal scatterer at the angle $\alpha+\varphi_0$, it is evident that the scatter far field due to the incident

Gaussian beam is a superposition, over the range $-(\frac{\pi}{2}-\varphi_0) \le \alpha \le (\frac{\pi}{2}-\varphi_0)$, of the plane wave scatter far fields with the amplitude E_0 in (2.5) replaced by the amplitude $E_0 A_0(\alpha)$. Thus, the beam wave scattered far field is given by

$$E_y^{(1),B}(\rho,\varphi) = \int_{-(\frac{\pi}{2}-\varphi_0)}^{(\frac{\pi}{2}-\varphi_0)} A_0(\alpha) E_y^{(1),PL}(\rho,\varphi;\alpha+\varphi_0)\, d\alpha\,, \tag{2.28}$$

Substituting (2.26) into (2.28) gives

$$E_y^{(1),B}(\rho,\varphi) = j\sqrt{\frac{2}{\pi}} E_0 \frac{e^{-j\left(k_0\rho+\pi/4\right)}}{\sqrt{k_0\rho}} S_{TE}^{(1),B}(\varphi,\varphi_0), \tag{2.29}$$

where

$$S_{TE}^{(1),B}(\varphi,\varphi_0) = \int_{-(\frac{\pi}{2}-\varphi_0)}^{(\frac{\pi}{2}-\varphi_0)} A_0(\alpha) S_{TE}^{(1),PL}(\varphi,\alpha+\varphi_0)\, d\alpha \tag{2.30}$$

and $E_y^{(1),B}(\rho,\varphi)$ is the first-order scatter field according to the CC-Theory for Gaussian beam scattering from PEC surface with finite rough surface segment.

Thus

$$\begin{aligned} S_{TE}^{(1),B}(\varphi,\varphi_0) = \frac{{k_0}^2 w_0}{2\sqrt{\pi}} \int_{-(\frac{\pi}{2}-\varphi_0)}^{(\frac{\pi}{2}-\varphi_0)} \left[e^{-\left[\frac{k_0 w_0 \sin\alpha}{2}\right]^2} \cos\alpha \right] \frac{\cos\varphi\cos(\alpha+\varphi_0)}{\cos\varphi+\cos(\alpha+\varphi_0)} \cdot e^{-jk_0\rho_0\cos\alpha} \\ \cdot \left\{ \int_{z_1=-L}^{L} \left[1-(1+{D_1}'^2) e^{jk_0 D_1(\cos\varphi+\cos(\alpha+\varphi_0))} \right] e^{jk_0 z_1(\sin\varphi-\sin(\alpha+\varphi_0))} dz_1 \right\} d\alpha \end{aligned} \tag{2.31}$$

for $-\frac{\pi}{2} \le \varphi \le \frac{\pi}{2}$, $-\frac{\pi}{2} \le \alpha+\varphi_0 \le \frac{\pi}{2}$ and φ_0 not near $\pm\frac{\pi}{2}$.

2.4 Specular Reflected Beam

For a plane wave incident upon a PEC scatter surface, the CC method designated the total field to consist of a primary field plus a series of scatter fields of which the lowest order one is referred to as the first-order scatter field. The primary field is defined to be the incident plane wave and the specularly reflected plane wave such that in the region $|z| > L$, $x \geq 0$ the primary field is identical to the primary field for the case of a planar metal surface. In Section 2.3, first-order scatter field was determined for an incident Gaussian beam scattered from a deterministic rough metal surface. In this section, the reflected Gaussian beam according to the CC method in $|z| > L$, $x \geq 0$ is determined for reflection from an infinite planar PEC surface. Since the incident Gaussian beam is a truncated spectrum of plane waves, the reflected field due to one plane wave will first be developed. This is then followed by the determination of the reflected Gaussian beam which is synthesized as a superposition of reflected plane waves.

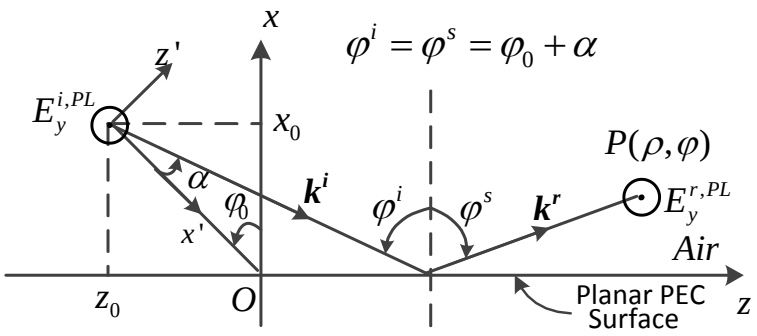

Figure 2.7 Incident and specular reflected TE polarized plane waves with a planar PEC surface at $x = 0$.

2.4.1 Reflected Plane Wave

Consider the TE polarized incident plane wave (2.5). In Figure 2.7, this plane wave propagates in the wave vector direction $\boldsymbol{k}^i$ and is incident at angle $\alpha+\varphi_0$ (measured positive from the positive x-axis) upon the infinite PEC planar surface. The incident plane wave gives rise to the TE polarized specularly reflected plane wave

$$\boldsymbol{E}^{r,PL}(x,z)=\hat{\boldsymbol{y}}E_y^{r,PL}=\hat{\boldsymbol{y}}E_0{}^r e^{-j\boldsymbol{k}^r\cdot\boldsymbol{R}}, \tag{2.32}$$

where the reflected wave vector and position vector (with origin at the antenna phase center) are given, respectively, by

$$\boldsymbol{k}^r=\hat{x}k_0\cos(\varphi_0+\alpha)+\hat{z}k_0\sin(\varphi_0+\alpha),\ \boldsymbol{R}=\hat{x}(x-x_0)+\hat{z}(z-z_0). \tag{2.33}$$

Using (2.33) in (2.32) gives the reflected TE polarized electric field plane wave

$$E_y^{r,PL}(x,z)=E_0{}^r e^{-jk_0\left[(x-x_0)\cos(\varphi_0+\alpha)+(z-z_0)\sin(\varphi_0+\alpha)\right]}. \tag{2.34}$$

At the perfectly conducting planar scatter surface, the tangential electric field must be zero, i.e.,

$$E_y^{i,PL}+E_y^{r,PL}=0 \text{ at } x=0,\ |z|<\infty. \tag{2.35}$$

Substituting (2.5) and (2.34) into (2.35) gives

$$E_0{}^r=-E_0{}^i e^{-jk_0\rho_0\cos\alpha}e^{-jk_0\left[x_0\cos(\varphi_0+\alpha)+z_0\sin(\varphi_0+\alpha)\right]}. \tag{2.36}$$

Substituting (2.36) into (2.34) gives the reflected electric field

$$E_y^{r,PL}(x,z)=-E_0{}^i e^{-jk_0\rho_0\cos\alpha}e^{-jk_0\left[x\cos(\varphi_0+\alpha)+z\sin(\varphi_0+\alpha)\right]}. \tag{2.37}$$

Recall that the incident Gaussian beam in (2.25) was constructed as a truncated spectrum of plane waves using the incident plane wave (2.5) with amplitude $E_0A_0(\alpha)$. In the same manner, the reflected Gaussian beam, represented as a superposition of reflected

plane waves, using the reflected plane waves (2.37) with amplitude $E_0 A_0(\alpha)$, is obtained as

$$E_y^{r,B}(x,z) = -E_0^{\,i} \int_{-(\frac{\pi}{2}-\varphi_0)}^{(\frac{\pi}{2}-\varphi_0)} A_0(\alpha) e^{-jk_0\rho_0\cos\alpha} e^{-jk_0\left[x\cos(\varphi_0+\alpha)+z\sin(\varphi_0+\alpha)\right]} d\alpha\,, \tag{2.38}$$

where $x_0 = \rho_0\cos\varphi_0$, $z_0 = -\rho_0\sin\varphi_0$, $x = \rho\cos\varphi$, $z = \rho\sin\varphi$ and $-\frac{\pi}{2} \le \varphi \le \frac{\pi}{2}$ $-\frac{\pi}{2} \le \varphi_0 \le \frac{\pi}{2}$ with φ_0 not near $\pm\varphi_0$.

Replacing the x and z coordinate variables with polar coordinate (ρ,φ) and using familiar trigonometric expressions, the reflected beam wave in (2.38) is written as

$$E_y^{r,B}(x,z) = -E_0^{\,i} \int_{-(\frac{\pi}{2}-\varphi_0)}^{(\frac{\pi}{2}-\varphi_0)} A_0(\alpha) e^{-jk_0\rho_0\cos\alpha} e^{-jk_0\rho\cos(\alpha-[\varphi-\varphi_0])} d\alpha\,. \tag{2.39}$$

Asymptotic evaluation of (2.39) for $k_0\rho$ large by the Method of Stationary Phase gives the reflected beam

$$E_y^{r,B}(\rho,\varphi) \approx E_y^{r,B}(\rho,\varphi) = j\sqrt{\frac{2}{\pi}} E_0 \frac{e^{-j\left(k_0\rho+\pi/4\right)}}{\sqrt{k_0\rho}} S_{TE}^{r,B}(\varphi,\varphi_0) \tag{2.40}$$

with reflected scatter pattern

$$S_{TE}^{r,B}(\rho,\varphi) = -\frac{1}{2}\sqrt{\pi}k_0\omega_0\cos(\phi-\phi_0) e^{-jk_0\rho_0} e^{-\frac{1}{2}\left[\frac{1}{2}(k_0\omega_0)^2 - jk_0\rho_0\right]\sin^2(\varphi-\varphi_0)} \tag{2.41}$$

Recall that the formula for the reflected beam field $E_y^{r,B}$ is asymptotic, which requires that $k_0\rho$ be large. It was also assumed for the incident Gaussian beam that φ_0 not be close to $\pm\pi/2$ and that condition (2.23), i.e., $e^{-(k_0 w_0\cos\varphi_0/2)^2} \ll 1$ be satisfied. The latter inequality

means that $(k_0 w_0/2)^2$ and, therefore, $k_0 w_0$ must also be sufficiently large. The composite requirement to obtain the far field to insure that the asymptotic evaluation remains the dominant effect is that $k_0\rho \gg (k_0 w_0/2)^2$. In other words, in the context of the plane wave spectrum representation, it is required that the "peaked" spectrum function $A_0(\alpha)$ does not become more important than the phase exponential in (2.39) in determining the far field.

The total beam wave scatter pattern is

$$S_{TE}^{TOT,B}(\varphi,\varphi_0) = S_{TE}^{(1),B}(\varphi,\varphi_0) + S_{TE}^{r,B}(\varphi,\varphi_0) \tag{2.42}$$

2.5 Accuracy Check – Power Conservation Criterion

Since the scatter surface is perfectly conducting, the total scattered and reflected power must equal the power carried by the incident beam, which means that conservation of power requires

$$P_B^i = P_B^{S,TOT}. \tag{2.43}$$

To measure how well this conservation of power criterion is satisfied in the CC method, define the % error

$$\varepsilon = \left(\frac{P_B^{S,TOT} - P_B^i}{P_B^i} \right) \times 100\%, \tag{2.44}$$

where the power per unit width of the incident beam is given by

$$P_B^i = \int_{z'=-\infty}^{\infty} \int_{y'=0}^{1} \boldsymbol{S}_{\boldsymbol{AV}}^{\boldsymbol{i}} \cdot \hat{\boldsymbol{x}}' dy' dz' = \frac{1}{2}\sqrt{\frac{\pi}{2}}\frac{w_0}{\eta_0}\left|E_0\right|^2, \tag{2.45}$$

and the total scattered power per unit width is

$$P_B^{S,TOT} = \int_{\varphi=-\pi/2}^{\pi/2} \int_{y=0}^{1} \boldsymbol{S}_{\boldsymbol{AV}}^{\boldsymbol{S,TOT}} \cdot \hat{\boldsymbol{\rho}} \rho d\varphi dy = \int_{\varphi=-\pi/2}^{\pi/2} \frac{1}{2\eta_0} \left| E_B^{S,TOT} \right|^2 \rho d\varphi, \tag{2.46}$$

where

$$\left|E_B^{S,TOT}\right|^2 = \frac{2}{\pi}\frac{1}{k_0\rho}\left|E_0\right|^2\left|S_{TE}^{(1),B}\left(\varphi,\varphi_0\right)+S_{TE}^{r,B}\left(\varphi,\varphi_0\right)\right|^2. \tag{2.46a}$$

Substituting (2.46a) into (2.46) gives

$$P_B^{S,TOT} = \frac{1}{\pi k_0\eta_0}\left|E_0\right|^2\int_{\varphi=-\pi/2}^{\pi/2}\left|S_{TE}^{(1),B}\left(\varphi,\varphi_0\right)+S_{TE}^{r,B}\left(\varphi,\varphi_0\right)\right|^2 d\varphi. \tag{2.47}$$

2.6 The Approximation First-Order Scatter Pattern

For sufficiently large k_0w_0, the double integrations in (2.31) for the first-order beam scatter pattern can be reduced to a single integration over the metal scatter surface. This is accomplished because α is small by using the following approximations:

(a) $\cos\left(\alpha+\varphi_0\right)\approx\cos\varphi_0$ in the amplitude terms. (2.48a)

(b) $\cos\alpha\approx 1-\frac{1}{2}\left(\sin^2\alpha\right)$ in the phase terms. (2.48b)

Substituting (2.48) into (2.31) and changing the order of the integrations give for the first-order beam scatter pattern

$$\begin{aligned} S_{TE}^{(1),B}\left(\varphi,\varphi_0\right) &= \frac{{k_0}^2w_0}{2\sqrt{\pi}}\frac{\cos\varphi\cos\varphi_0}{\cos\varphi+\cos\varphi_0}e^{-jk_0\rho_0}\int_{z_1=-L}^{L}e^{jk_0z_1\left(\sin\varphi-\sin\varphi_0\right)} \\ &\cdot\left\{I_1-e^{jk_0D_1\left(\cos\varphi+\cos\varphi_0\right)}\left(1+{D_1}'^2\right)I_2\right\}dz_1 \end{aligned} \tag{2.49}$$

where

$$I_1 = \int_{\alpha=-\alpha_0^+}^{\alpha_0^+} e^{-\left[\frac{{k_0}^2w_0^2}{4}-\frac{1}{2}jk_0\rho_0-\frac{1}{2}jk_0z_1\sin\varphi_0\right]\sin^2\alpha}\,\mathrm{e}^{-jk_0z_1\cos\varphi_0\sin\alpha}\cos\alpha d\alpha \tag{2.49a}$$

$$I_2 = \int_{\alpha=-\alpha_0^+}^{\alpha_0^+} e^{-\left[\frac{{k_0}^2w_0^2}{4}-\frac{1}{2}jk_0\rho_0-\frac{1}{2}jk_0z_1\sin\varphi_0+\frac{1}{2}jk_0D_1\cos\varphi_0\right]\sin^2\alpha}\,e^{-j\left[k_0z_1\cos\varphi_0+k_0D_1\sin\varphi_0\right]\sin\alpha}\cos\alpha d\alpha \tag{2.49b}$$

Using the change in variable $u = \sin\alpha$, the integrations over α in I_1 and I_2 transform to integrations over u. Since $k_0 w_0$ is large, the integrand decays and the range of integration over u can be extended over the infinite range $-\infty < u < \infty$ because the extended portions do not alter the valuation of the integrals. The integrals over the infinite range is then evaluated in closed form to give the approximate beam scatter pattern

$$S_{TE}^{(1),B^{Approx}}\left(\varphi,\varphi_0\right) = k_0 \frac{\cos\varphi\cos\varphi_0}{\cos\varphi+\cos\varphi_0} e^{-jk_0\rho_0} \int_{z_0=-L}^{L} e^{jk_0 z_1(\sin\varphi-\sin\varphi_0)} \cdot \left[\hat{I}_1 - \left(1+D_1{}'^2\right) e^{jk_0 D_1(\cos\varphi+\cos\varphi_0)} \hat{I}_2\right] dz_0 \tag{2.50}$$

where

$$I_1 = \frac{exp\left\{-\frac{\left(z_0\cos\varphi_0/w_0\right)^2}{1-j\left(\frac{\rho_0+z_1\sin\varphi_0}{k_0 w_0{}^2/2}\right)}\right\}}{\left[1-j\left(\frac{\rho_0+z_1\sin\varphi_0}{k_0 w_0{}^2/2}\right)\right]^{1/2}} \tag{2.50a}$$

$$I_2 = \frac{exp\left\{\frac{-\left(\frac{z_1}{w_0}\cos\varphi_0+\frac{D_1}{w_0}\sin\varphi_0\right)^2}{1-j\left(\frac{\rho_0+z_1\sin\varphi_0-D_1\cos\varphi_0}{k_0 w_0{}^2/2}\right)}\right\}}{\left[1-j\left(\frac{\rho_0+z_1\sin\varphi_0-D_1\cos\varphi_0}{k_0 w_0{}^2/2}\right)\right]^{1/2}} \tag{2.50b}$$

CHAPTER 3

FORMULATION AND SOLUTION OF BEAM WAVE SCATTER PROBLEM BY USE OF THE METHOD OF MOMENTS

In this chapter, the well known numerical method in electromagnetic called the Method of Moment [5] is developed for comparison. An integral equation for the surface current induced on a perfectly conducting scatterer is derived from boundary conditions on the electric field. To solve the integral equation by the MOM, a set of expansion functions and a testing procedure are developed and used to derive the elements of the moment matrix. The problem is reduced to a consideration of the fields over a single period. Finally, the numerical computation of the moment matrix elements is discussed.

3.1 MOM Using Image Theory

The scatter surface under investigation is shown in Figure 3.1. It is a perfectly conducting surface that lies along the z-axis and has a sinusoidal one-dimensional roughness profile $x = D(z) = D_0\left[1 - \sin^2\left(\frac{N_b}{2}\pi\frac{z}{L}\right)\right]$ in the region, $|z| \le L$, but is planar ($D = 0$) over the regions $|z| \ge L$, where N_b is the number of bumps. A TE polarized beam wave is assumed incident upon this rough metal surface. The MOM is implemented to find the scattered field after applying image theory. For convenience, the simpler scatter surface shown in Figure 3.2 – that of a single bump on an infinite PEC planar surface - is used to illustrate how image theory is implemented. Extension to more scatter surfaces with several bumps is straightforward.

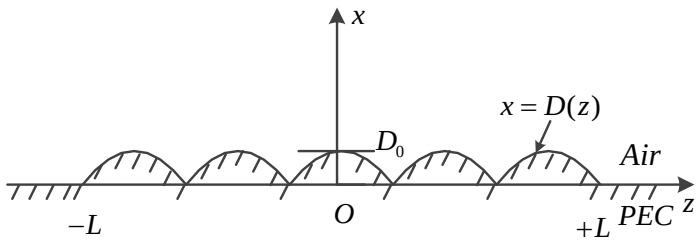

Figure 3.1 Deterministic rough PEC scatter surface.

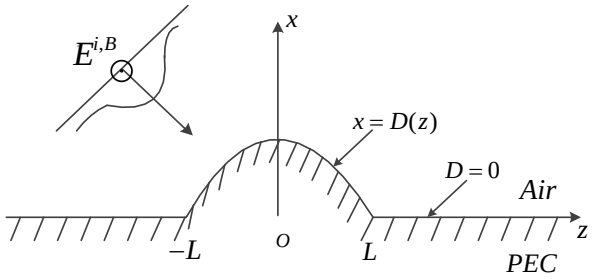

Figure 3.2 PEC scatter surface with one bump illuminated by an incident TE polarized Gaussian beam.

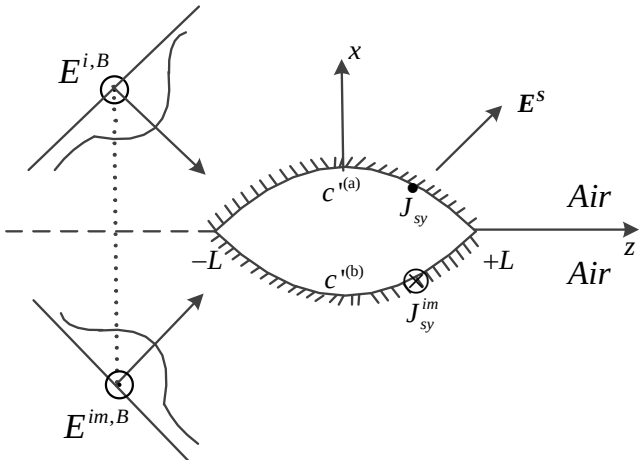

Figure 3.3 Incident and image TE polarized Gaussian beams and surface current densities.

In Figure 3.2, the TE polarized Gaussian beam with an electric field in the +y direction $\boldsymbol{E}^{i,B} = \hat{\boldsymbol{y}}E_y^{i,B}$ is shown incident upon the infinite PEC scatterer with one bump. In Figure 3.3, the equivalent image problem is shown, which can be understood by placing an infinite PEC planar surface along the entire z-axis under the infinite one bump PEC scatter surface. Image theory predicts that the image problem of Figure 3.3 includes the original

incident Gaussian beam wave field $\boldsymbol{E}^{\boldsymbol{i,B}} = \hat{\boldsymbol{y}} E_y^{i,B}$, an image incident TE polarized Gaussian beam with an electric field in the –y direction $\boldsymbol{E}^{\boldsymbol{i,B}} = \hat{\boldsymbol{y}} E_y^{im,B}$, the surface current density $\boldsymbol{J}_{\boldsymbol{s}} = \hat{\boldsymbol{y}} J_{sy}$ in the + y direction that was induced on the surface of the original PEC single bump and its image surface current density $\boldsymbol{J}_{\boldsymbol{s}}^{\boldsymbol{im}} = \hat{\boldsymbol{y}} J_{sy}^{im}$ that flows in the –y direction. The direction of the current flow is determined from the boundary condition $\boldsymbol{J}_{\boldsymbol{s}} = \hat{\boldsymbol{n}} \, x \, \boldsymbol{H}$ at the PEC surface, i.e., at $x = D(\mathrm{z}), |z| < \infty$, where $\hat{\boldsymbol{n}}$ is the unit normal vector directed into the air region from the PEC. The incident fields and induced surface current densities in the image problem are all located in air. The field solution to the image problem is equivalent to the field solution to the one bump scatter problem in Figure 3.2 in the physical regions $x \geq D(\mathrm{z})$, $|z| < \infty$. Note that in these regions, the image incident Gaussian beam is identical to the reflected Gaussian beam from an infinite planar PEC surface that was developed in Section 2.4 and that the reference MOM scatter field is approximated by the CC first-order scatter field due to the rough scatter segment only.

The boundary condition that the tangential electric field at the PEC surfaces in Figure 3.2 be zero is written as

$$E_y = 0 \text{ at } x = D(\mathrm{z}), \ |z| < \infty \tag{3.1}$$

where E_y is the total electric field at the surface of the PEC. Since the field solution to the image problem of Figure 3.3 is equivalent to the field solution of the original one bump problem of Figure 3.2 (in the region above and at the bump), the field at the surface containing the induced current $\boldsymbol{J}_{\boldsymbol{s}} = \hat{\boldsymbol{y}} J_{sy}$ in the image problem must also satisfy the boundary condition (3.1) . Because of image theory, the total electric field in the image

problem of Figure 3.3 is given by $E_y = E_y^{i,B} + E_y^{im,B} + E_y^{S,B}$, the boundary condition (3.1) becomes

$$E_y^{i,B} + E_y^{im,B} + E_y^{S,B} = 0 \text{ at } x = \pm D(\text{z}),\ |z| < \infty . \tag{3.2}$$

The scatter field $E_y^{S,B}$ is due only to the surface current densities on the bump and its image because the induced surface current density and its image on the planar PEC portions of the surface give zero current, i.e., $J_{sy} + J_{sy}^{im} = 0$ over $|z| \geq L, x = 0$.

The incident Gaussian beam wave field in (3.2) is given in (2.25) by

$$E_y^{i,B}(x,z) = E_0 \int_{-(\frac{\pi}{2}-\varphi_0)}^{(\frac{\pi}{2}-\varphi_0)} A_0(\alpha) e^{-jk_0\rho_0\cos\alpha} e^{jk_0 x\cos(\varphi_0+\alpha) - jk_0 z\sin(\varphi_0+\alpha)} d\alpha , \tag{3.3}$$

which consists of a spectrum of plane waves that propagate in the wave vector directions

$$\boldsymbol{k}^i = -\hat{\boldsymbol{x}} k_0 \cos(\alpha+\varphi_0) + \hat{\boldsymbol{z}} k_0 \sin(\alpha+\varphi_0),\ |\alpha| \leq \alpha_0^+ \equiv \pi/2 - \varphi_0 . \tag{3.3a}$$

The image incident Gaussian beam wave field is given by

$$E_y^{im,B}(x,z) = -E_0 \int_{-(\frac{\pi}{2}-\varphi_0)}^{(\frac{\pi}{2}-\varphi_0)} A_0(\alpha) e^{-jk_0\rho_0\cos\alpha} e^{-jk_0 x\cos(\varphi_0+\alpha) - jk_0 z\sin(\varphi_0+\alpha)} d\alpha , \tag{3.4}$$

which consists of a spectrum of plane waves that propagate in the wave vector directions

$$\boldsymbol{k}^{im} = \hat{\boldsymbol{x}} k_0 \cos(\alpha+\varphi_0) + \hat{\boldsymbol{z}} k_0 \sin(\alpha+\varphi_0),\ |\alpha| \leq \alpha_0^+ \equiv \pi/2 - \varphi_0 . \tag{3.4a}$$

The scatter field is obtained from the surface current densities and is given by

$$E_y^{S,B}(\boldsymbol{\rho}) = -\frac{k_0\eta_0}{4} \oint_{C'} J_{sy}(\boldsymbol{\rho}') H_0^{(2)}\left(k_0|\boldsymbol{\rho} - \boldsymbol{\rho}'|\right) dc' , \tag{3.5}$$

where use has been made of the two-dimensional free space Green's function which is proportional to the Hankel function of the second kind of order zero [5]. The position vector $\boldsymbol{\rho}'$ locates points on the surface occupied by the current density and its image while the position vector $\boldsymbol{\rho}$ reaches observations points in the physical space $x \geq D(\text{z})$, $|z| \geq L$;

refer to Figure 3.4. η_0 is the free space intrinsic impedance. The integration path in (3.5) runs along the contour $c' = c'^{(a)} + c'^{(b)}$ which is shown in Figure 3.3.

Substituting (3.3), (3.4) and (3.5) into (3.2) gives the electric field integral equation (EFIE) for the unknown current densities $J_{sy}(\boldsymbol{\rho}')$

$$E_0 \int_{-(\frac{\pi}{2}-\varphi_0)}^{(\frac{\pi}{2}-\varphi_0)} A_0(\alpha) e^{-jk_0\rho_0\cos\alpha} \left\{ e^{jk_0\left[x\cos(\alpha+\varphi_0)-z\sin(\alpha+\varphi_0)\right]} - e^{-jk_0\left[x\cos(\alpha+\varphi_0)+z\sin(\alpha+\varphi_0)\right]} \right\} d\alpha = \frac{k_0\eta_0}{4} \oint_{C'} J_{sy}(\boldsymbol{\rho}') H_0^{(2)}\left(k_0\left|\boldsymbol{\rho}-\boldsymbol{\rho}'\right|\right) dc' \quad . \quad (3.6)$$

In (3.6) both the source point and the observation point are located at points on the surface occupied by the current density and its image, which for the simple geometry of Figure 3.6 means on the surface of the bump and on the image surface of the bump. In general, the observation point is located on the surface defined by the equations $x = \pm D(z),\ |z| \le L$. Care must be used in making calculations when the source point $P'(\rho', \theta')$ is near the observation point $P(\rho, \theta)$.

The EFIE (3.6) is an integral equation for the unknown surface current density that appears in the integrand. To solve such an equation, numerical techniques are used. We approximate the unknown current density $J_{sy}(\boldsymbol{\rho}')$ in (3.6) over the path $c' = c'^{(a)} + c'^{(b)}$ by means of a piecewise constant function (a staircase representation). As illustrated in Figure 3.5, the above path is divided into 2N segments and each segment has a corresponding subspace projection on the z-axis of length $\Delta = 2L/2N$, with the center of the n^{th} segment designated z_n and where

$$z_n = -L + \Delta(n - 1/2),\ \text{n=1,2, …, 2N.} \quad (3.7)$$

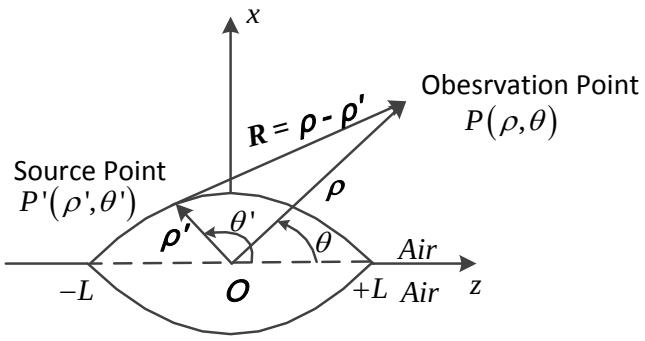

Figure 3.4 Geometry of the surfaces occupied by the current densities and the coordinate designations of source and observation points.

To find the unknown induced current density J_{sy}, the first step is to approximate it by a series of known expansion functions $g_n(\boldsymbol{\rho}')$ such that

$$J_{sy}(\boldsymbol{\rho}') = \sum_{n=1}^{2N} a_n g_n(\boldsymbol{\rho}'), \tag{3.8}$$

where the expansion coefficients a_n are unknown constants. For simplicity, the expansion functions $g_n(\boldsymbol{\rho}')$ are chosen to be a set of orthogonal pulse functions given by

$$g_n(\boldsymbol{\rho}') = \begin{cases} 1, z \in (z_n - \Delta/2, z_n + \Delta/2) \\ 0, otherwise \end{cases}, \tag{3.9}$$

The expansion of the current density in terms of pulse functions in (3.8) is a "staircase" approximation where the current is divided into 2N segments of length Δ.

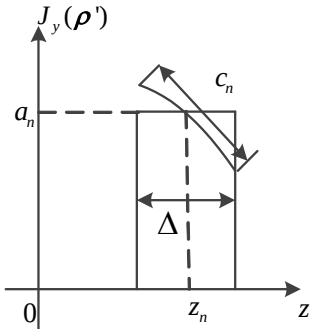

Figure 3.5 A pulse approximation of one segment of the current density.

In Figure 3.5 within the n^{th} segment $\left(z_n-\Delta/2, z_n+\Delta/2\right)$, $J_{sy}\left(\boldsymbol{\rho}'\right)$ is approximated by the constant a_n; that is, $J_{sy}\left(\boldsymbol{\rho}'\right)=a_n$ for $z\in\left(z_n-\Delta/2, z_n+\Delta/2\right)$.

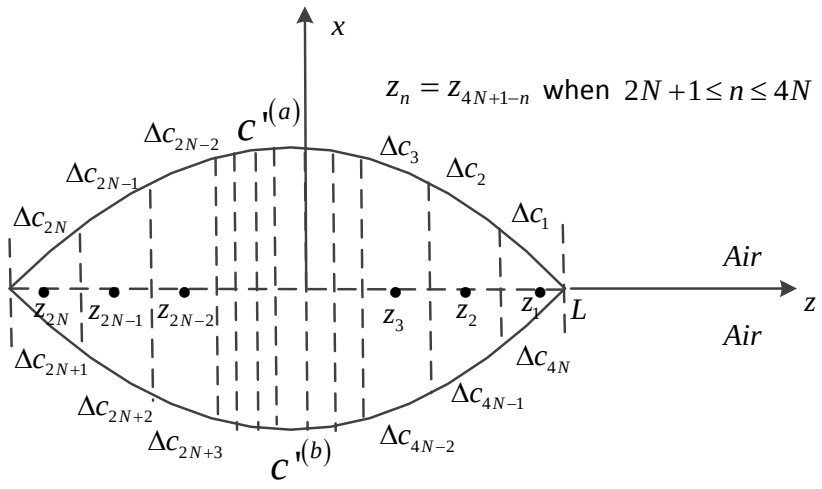

Figure 3.6 Discretizations between points on the coutours and their projections onto z-axis.

A similar situation occurs over the path $c'^{(b)}$ as shown in Figure 3.6, where $2N+1\le n\le 4N$, $x=-D(z)$ and $J_{sy}^{im}\left(\boldsymbol{\rho}'\right)=-J_y\left(\boldsymbol{\rho}'\right)$ with

$$\Delta c_n=\sqrt{\Delta x_n{}^2+\Delta z_n{}^2}=\sqrt{1+(\frac{\Delta x_n}{\Delta z_n})^2}\,\Delta z_n=\sqrt{1+(D'(z=z_n))^2}\,\Delta z_n, \text{ for n=1, 2, 3,…, 4N.(3.10)}$$

Substituting pulse expansion functions for the unknown currents into (3.6) gives

$$E_y^{i,B}+E_y^{im,B}=-E_y^S\left(\boldsymbol{\rho}\right)=\frac{k_0\eta_0}{4}\oint_C J_{sy}(\boldsymbol{\rho}')H_0^{(2)}\left(k_0\left|\boldsymbol{\rho}-\boldsymbol{\rho}'\right|\right)dc',$$

$$=\frac{k_0\eta_0}{4}\int_{c'^{(a)}}\left(\sum_{n=1}^{2N}a_n^{(a)}g_n\left(\boldsymbol{\rho}'\right)\right)H_0^{(2)}\left(k_0\left|\boldsymbol{\rho}-\boldsymbol{\rho}_n'\right|\right)dc'+\frac{k_0\eta_0}{4}\int_{c'^{(b)}}\left(\sum_{n=2N+1}^{4N}a_n^{(b)}g_n\left(\boldsymbol{\rho}'\right)\right)H_0^{(2)}\left(k_0\left|\boldsymbol{\rho}-\boldsymbol{\rho}_n'\right|\right)dc' \quad (3.11)$$

where $E_y^{i,B}$ and $E_y^{im,B}$ are known and given by equations (3.3) and (3.4).

Interchanging the order of the integration and the summation in (3.11) gives

$$E_y^{i,\mathrm{B}} + E_y^{im,B} = \sum_{n=1}^{4N} a_n \frac{k_0\eta_0}{4} \oint_{c'} g_n(\boldsymbol{\rho}') H_0^{(2)}\left(k_0 \left|\boldsymbol{\rho} - \boldsymbol{\rho}_n'\right|\right) dc' \tag{3.12}$$

Since the n^{th} pulse is unity for $z \in (z_n - \Delta/2, z_n + \Delta/2)$ and is zero outside this interval, (3.12) reduces to

$$E_y^{i,\mathrm{B}} + E_y^{im,B} = \sum_{n=1}^{4N} a_n \frac{k_0\eta_0}{4} \int_{c_n-\Delta/2}^{c_n+\Delta/2} H_0^{(2)}\left(k_0 \left|\boldsymbol{\rho} - \boldsymbol{\rho}_n'\right|\right) dc \approx \sum_{n=1}^{4N} \frac{k_0\eta_0}{4} H_0^{(2)}\left(k_0 \left|\boldsymbol{\rho} - \boldsymbol{\rho}_n'\right|\right) \Delta c_n \cdot a_n \tag{3.13}$$

which, for convenience, is expressed as

$$E_y^{i,B}(\mathrm{z}) + E_y^{im,B}(\mathrm{z}) = \sum_{n=1}^{4N} A_n Y_n(z) = A_1 Y_1(z) + A_2 Y_2(z) + \cdots + A_{4N} Y_{4N}(z) \tag{3.14}$$

where $A_n \equiv a_n$ and

$$Y_n(z) = \Delta c_n \cdot \frac{k_0\eta_0}{4} H_0^{(2)}\left(k_0 \left|\boldsymbol{\rho} - \boldsymbol{\rho}_n'\right|\right) \tag{3.14a}$$

Equation (3.14) reflects the fact that the problem of determining $J_{sy}(\boldsymbol{\rho}')$ at all points of the surface has been replaced by that of computing the 4N constants $A_n \equiv a_n$. Clearly, (3.14) is a single equation containing 4N unknowns and it cannot be solved for the constants A_n in its present form.

The exact solution $J_{sy}(\boldsymbol{\rho}')$ of the integral equation (3.6) ensures that the right- and left-hand sides of this equation are equal at every point of the surface, but any approximate solution does not ensure equality at all points. A solution is sought which is as nearly equal as possible to $J_{sy}(\boldsymbol{\rho}')$ in the sense that, at specified match points at the surface, (3.14), which is an approximation to (3.6), is forced to hold exactly. The center point z_n of each

segment $\left(z_n - \Delta/2, z_n + \Delta/2\right)$ is selected as a match point but, to distinguish it from the z_n employed in (3.7)-(3.14), the match point is designated z_m where

$$z_m = -L + \Delta(m - \frac{1}{2}),\ \text{m=1, 2, …, 2N}$$

$$z_m = z_{4N+1-m},\ \text{m=2N+1,2N+2, …, 4N} \tag{3.15}$$

and the observation point $\rho = \rho_m$ with $\left(x, y\right) = \left(x_m, y_m\right)$.

Thus, at each match points z_m, (3.14) is enforced to give the linear system of equations

$$\begin{aligned}
&A_1 Y_1(z_1) + A_2 Y_2(z_1) + \cdots A_n Y_n(z_1) + \cdots + A_{4N} Y_{4N}(z_1) = E_y^{i,\mathrm{B}}(\mathrm{z}_1) + E_y^{im,B}(\mathrm{z}_1) \\
&A_1 Y_1(z_2) + A_2 Y_2(z_2) + \cdots A_n Y_n(z_2) + \cdots + A_{4N} Y_{4N}(z_2) = E_y^{i,B}(\mathrm{z}_2) + E_y^{im,B}(\mathrm{z}_2) \\
&\quad\vdots \qquad\qquad\qquad \vdots \qquad\qquad\qquad \vdots \\
&A_1 Y_1(z_m) + A_2 Y_2(z_m) + \cdots A_n Y_n(z_m) + \cdots + A_{4N} Y_{4N}(z_m) = E_y^{i,B}(\mathrm{z}_m) + E_y^{im,B}(\mathrm{z}_m) \\
&\quad\vdots \qquad\qquad\qquad \vdots \qquad\qquad\qquad \vdots \\
&A_1 Y_1(z_{4N}) + A_2 Y_2(z_{4N}) + \cdots A_n Y_n(z_{4N}) + \cdots + A_{4N} Y_{4N}(z_{4N}) = E_y^{i,B}(\mathrm{z}_{4N}) + E_y^{im,B}(\mathrm{z}_{4N})
\end{aligned} \tag{3.16}$$

Note that Y_n is a function only of z and that, with a discrete value z_m substituted into this function, $Y_n\left(z_m\right)$ is a known value which can in principle be computed from (3.14a). Hence, (3.16) is a set of 4N linear equations with constant coefficients $Y_n\left(z_m\right)$ and unknowns A_n. Since $E_y^{i,B}(\mathrm{z}_m) + E_y^{im,B}(\mathrm{z}_m)$ is known, then A_n can be determined by standard techniques.

Equation (3.16) can be written as

$$\sum_{n=1}^{4N} A_n Y_{mn} = H_m, \text{ m=1,2,…,4N,} \tag{3.17}$$

where $Y_{mn} = Y_n(z_m) = \frac{k_0\eta_0}{4} H_0^{(2)}\left(k_0\left|\boldsymbol{\rho_m} - \boldsymbol{\rho_n}'\right|\right)$ and $H_m = E_y^{i,B}(z_m) + E_y^{im,B}(z_m)$ are known quantities, and $R_{mn} = \left|\boldsymbol{\rho_m} - \boldsymbol{\rho_n}'\right| = \sqrt{(x_m - x_n)^2 + (z_m - z_n)^2}$.

Alternatively, (3.17) can be written as a matrix equation

$$\left[Y_{mn}\right]\left[A_n\right] = \left[H_m\right] \tag{3.18}$$

where $\left[A_n\right]$ and $\left[H_m\right]$ are column vectors with 4N elements and $\left[Y_{mn}\right]$ is an $4N \times 4N$ square matrix. Thus, we can get

$$\left[A_n\right] = \left[Y_{mn}\right]^{-1}\left[H_m\right], \tag{3.19}$$

where $\left[Y_{mn}\right]^{-1}$ is the inverse of $\left[Y_{mn}\right]$, so the approximate solution is available as

$$J_{sy}(\boldsymbol{\rho'}) \approx \sum_{n=1}^{4N} A_n g_n(\boldsymbol{\rho'}). \tag{3.20}$$

CHAPTER 4

NUMERICAL RESULTS

Using the first-order CC theory, TE normalized power scatter patterns have been computed and plotted for a number of deterministic rough surfaces of the finite periodic type. The results are shown in Figures 4.3 to 4.15, where these patterns are compared to the scatter patterns obtained by an electric field integral equation/MOM technique. The Q_1, Q_2 and Q_3 values indicated in the Figures 4.3-4.6 refer to an error criterion for the first-order CC-method that was developed in [1]. Conservation of power criterion (2.44) is also shown in each figure.

4.1 Scatter Patterns of Deterministic Rough Surface

Figure 4.1 displays an example of a scatter surface profile of finite periodicity; it has five bumps $(N_b = 5)$ and is described by the expression

$$D(z) = \begin{cases} D_0\left[1-\sin^2\left(\frac{5\pi}{2}\frac{z}{L}\right)\right] & \text{for} \quad |z| \le L \\ 0 & \text{for} \quad |z| > L \end{cases}, \tag{4.1}$$

which satisfies the conditions that $D(\pm L)=D'(\pm L)=0$ and is plotted for $2L= 8\lambda$.

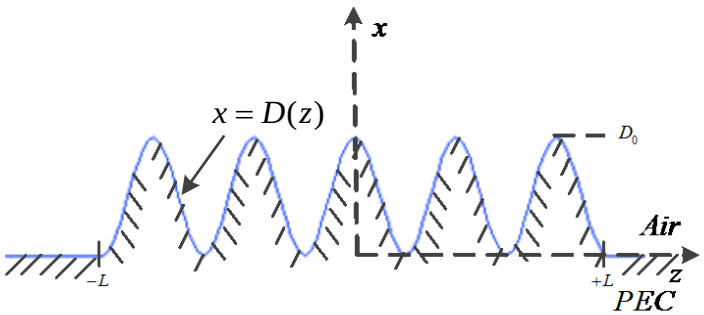

Figure 4.1 Surface Profile $x = D(z)$ with 5 bumps.

Figures 4.2-4.15 display curves of a normalized power scatter pattern for the surface profile (4.1) plotted versus scatter angle φ. A TE polarized electric field Gaussian beam wave excited by an aperture antenna is assumed to be incident in the air half-space and the scatter pattern is calculated for the PEC scatter surface having the surface profile of Figure 4.1. Calculations were performed by using the first-order correction current solution and the method of moments (MOM) solution of an electric field integral equation formulation of the problem, which were discussed in Chapter 2 and 3, respectively.

The normalized power scatter pattern is defined by the expression

$$R^{B,TOT}(\varphi,\varphi_0) = \frac{\pi\rho S_{AV}^{S,TOT}(\rho,\varphi;\varphi_0)}{P_B^i} \quad \text{for} \quad \rho\to\infty, \tag{4.2}$$

where $S_{AV}^{S,TOT}(\rho,\varphi;\varphi_0)$ is the time-averaged power density (Poynting vector) of the total scattered beam field at a far distance from the origin, i.e., for $\rho=(x^2+z^2)\to\infty$ and P_B^i is the total power per unit width of an incident beam.

For the Gaussian incident beam radiated by the aperture antenna and scattered by the metal surface in Figure 4.1, the incident power per width is

$$P_B^i = \int_{z'=-\infty}^{\infty}\int_{y'=0}^{1} \boldsymbol{S_{AV}^i}\cdot\hat{\boldsymbol{x}}'dy'dz' = \frac{1}{2}\sqrt{\frac{\pi}{2}}\frac{w_0}{\eta_0}\left|E_0\right|^2 \quad \text{for } k_0w_0\gg 1, \tag{4.3}$$

and the total scattered time-averaged power density in the far field is

$$S_{AV}^{S,TOT}(\rho,\varphi;\varphi_0) = \frac{1}{2\eta_0}\left|E_y^{S,TOT}\right|^2 \quad \text{for } \rho\to\infty \tag{4.4}$$

For the CC solution method, the total scattered field is

$$E_{y,CC}^{S,TOT} = E_y^{(1),\mathrm{B}} + E_y^{r,B}, \tag{4.5}$$

where as for the moment method solution using image theory, the total scattered field is

$$E_{y,MM}^{S,TOT} = E_y^{S,B} + E_y^{im,B}. \tag{4.6}$$

Comparing (4.5) and (4.6) shows that the reflected beam in the CC method is identical to the image beam in the moment method and that the first-order scatter field in the CC method approximates the scatter field derived using MOM.

Usually, scatter patterns are plotted using radar cross section (RCS). However, a RCS for the infinite two-dimensional scatter surface of Figure 4.1 does not make sense. Such a formula would make sense for a target of finite cross-section (which may be many wavelengths long) and an incident field near the target that could be regarded in good approximation as a plane wave. Both these conditions are not satisfied for the scatter problem under consideration, which involves an infinite PEC scatter surface and a Gaussian incident beam.

For the CC solution method, substitution of (4.3) and (4.5) into (4.2) using the first-order scatter field (2.29) and the reflected beam field (2.40) yield the normalized power scatter pattern for TE polarization expressed in terms of the field scatter patterns $S_{TE,CC}^{S,TOT}(\varphi,\varphi_0) \equiv S_{TE,CC}^{(1),\mathrm{B}} + S_{TE,CC}^{r,B}$ as

$$R_{TE,CC}^{B,TOT} = 2\sqrt{\frac{2}{\pi}}\frac{1}{k_0 w_0}\left|S_{TE}^{(1),\mathrm{B}} + S_{TE}^{r,B}\right|^2 \quad \text{for} \quad \rho \to \infty,\ k_0 w_0 \gg 1 \tag{4.7a}$$

and additional normalized power pattern formulas are defined by

$$R_{TE,CC}^{\mathrm{S},B} = 2\sqrt{\frac{2}{\pi}}\frac{1}{k_0 w_0}\left|S_{TE}^{(1),\mathrm{B}}\right|^2, \tag{4.7b}$$

$$R_{TE,CC}^{\mathrm{r},B} = 2\sqrt{\frac{2}{\pi}}\frac{1}{k_0 w_0}\left|S_{TE}^{r,B}\right|^2. \tag{4.7c}$$

In the moment method solution presented in Chapter 3 using image theory, (3.5) gives the scattered electric field at an arbitrary point in space due to the current densities in Figure 3.3 in terms of the Hankel function of the second kind of order zero

$$E_y^{S,B}(\boldsymbol{\rho}) = -\frac{k_0\eta_0}{4}\oint_{C'} J_{sy}(\boldsymbol{\rho}')H_0^{(2)}\left(k_0\left|\boldsymbol{\rho}-\boldsymbol{\rho}'\right|\right)dc' \tag{4.8}$$

Using the asymptotic form of the Hankel function at large distances from the scatter in (4.8),

$$H_0^{(2)}\left(k_0\left|\boldsymbol{\rho}-\boldsymbol{\rho}'\right|\right) = \sqrt{\frac{2j}{\pi k_0\rho}}e^{-jk_0(\rho-\rho')} \text{ for } \rho\to\infty, \tag{4.9}$$

and substituting the resultant scattered far electric field into (4.4) yields the MOM scattered power density in the far field

$$S_{AV}^{S} = \frac{k_0\eta_0}{16\pi\rho}\left|\oint_{c'} J_{sy}\left(\boldsymbol{\rho}'\right)e^{jk_0\rho'}dc'\right|^2 \tag{4.10}$$

Using the moment method solution for the surface current density $J_{sy}\left(\boldsymbol{\rho}'\right)$ allows for the numerical evaluation of the integral in (4.10), which can be written as

$$I \equiv \left|\oint_{c'} J_{sy}\left(\rho'\right)e^{jk_0\rho'}dc'\right| = \left|\sum_{n=1}^{4N} A_n e^{jk_0\rho_n'}\Delta c_n\right|, \tag{4.11}$$

where the expansion coefficients A_n were found via the moment method in Chapter 3. Substituting (4.3) and (4.10) into (4.2) gives the normalized power scatter pattern

$$R_{TE,MM}^{S,B} = \frac{1}{8}\sqrt{\frac{2}{\pi}}\frac{k_0{\eta_0}^2}{w_0}\frac{|I|^2}{|E_0|^2} \quad \text{for} \quad \rho\to\infty,\ k_0w_0 \gg 1, \tag{4.12}$$

where E_0 is set to unity for all figures.

Note that the power scatter pattern in (4.12) is given without inclusion of the reflected power scatter pattern, while the power scatter pattern in (4.7) includes the reflected beam.

4.2 Numerical Results

In the numerical simulations using the MOM, spatial resolution (2N), which is the number of the projected segment onto the z axis of the induced current density in the x positive region in the simulation is set to 600 evenly spaced data points over the surface width $|z| \le L$, which is chosen after confirming that no changes occur in the results by increasing 2N from 400 to 800 is shown in Figure 4.2. In Figures 4.3a, 4.4a, 4.5a and 4.6a, four curves are drawn which give the normalized power scatter pattern of the CC-Exact and CC-Approx formulas via 4.7(b), the MOM solution via (4.12) and the total scatter patter given by CC-Exact with the reflected beam via 4.7(a) for $N_b = 5$. Figures 4.3b, 4.4b, 4.5b and 4.6b, in particularly, show why the total power scatter pattern is maximum in specularly reflected direction. It is because of the inclusion of the specularly reflected beam.

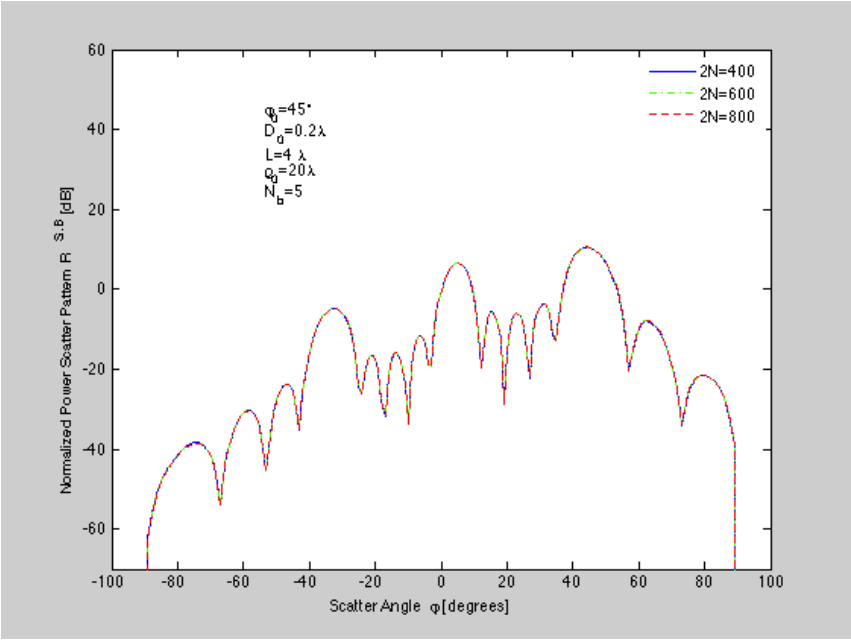

Figure 4.2 Normalized power scatter pattern $R_{TE,MM}^{S,B}$ versus scatter angle for the PEC scatter surface in Figure 4.1 of different spatial resolution (2N) to show convergence of the MOM solutions.

In Figures 4.3-4.6, the scatter width $2L = 8\lambda$, but the profile height D_0 varies from 0.1λ to 0.7λ. In each figure, the distance from the antenna phase center to the origin is $\rho_0 = 20\lambda$. The antenna main beam direction is $\varphi_0 = 45^\circ$.

In [1], an heuristic "error criterion" was developed to predict when the CC method is expected to remain valid, which is

$$Q = Q_1 + Q_2 = 2\left[\left\langle D'^2 \right\rangle + \left\langle D'^4 \right\rangle + \frac{1}{2k^2}\left\langle D''^2 \right\rangle\right] \ll 1 \tag{4.13}$$

where $Q_1 = 2\left[\left\langle D'^2 \right\rangle + \left\langle D'^4 \right\rangle\right]$ and $Q_2 = \left\langle D''^2 \right\rangle / k^2$ characterize the average slope and average curvature, respectively, of the scatter surface. Comparison of the first-order scatter pattern of the CC method with the integral equation/ method of moments (MOM) technique show in Figures 4.3a and 4.4a that good agreement is obtained for Q smaller than one, but show deviation in Figures 4.5a and 4.6a for Q greater than one. Although the criterion (4.13) was derived for a single incident plane wave in [1], it is valid for the incident beam wave since the beam wave is a superposition of plane waves. Figures 4.5 and 4.6 with high Q values also have larger conservation of power errors ε, which means that the CC method is not expected to be accurate.

The MOM simulations require considerable computational resources. On a 2.5 GHz Intel Core i5 CPU with 4 GB of memory, a MOM simulation takes about 4 hours as compared to a simulation using the CC method which takes 30 minutes.

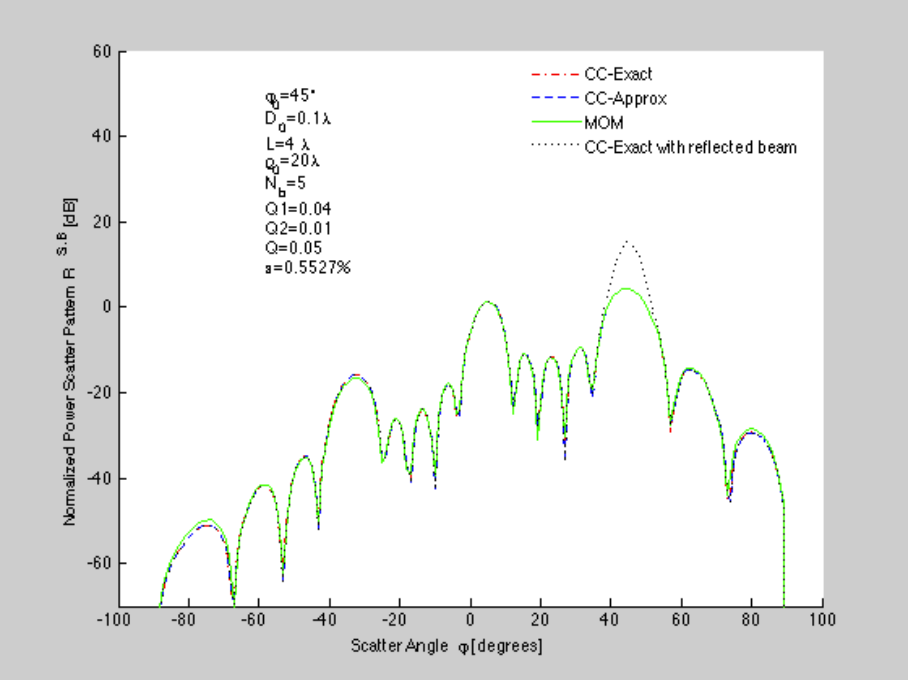

Figure 4.3a Normalized power scatter pattern versus scatter angle for the PEC scatter surface in Figure 4.1 of length $2L = 8\lambda$ and height $D_0 = 0.1\lambda$.

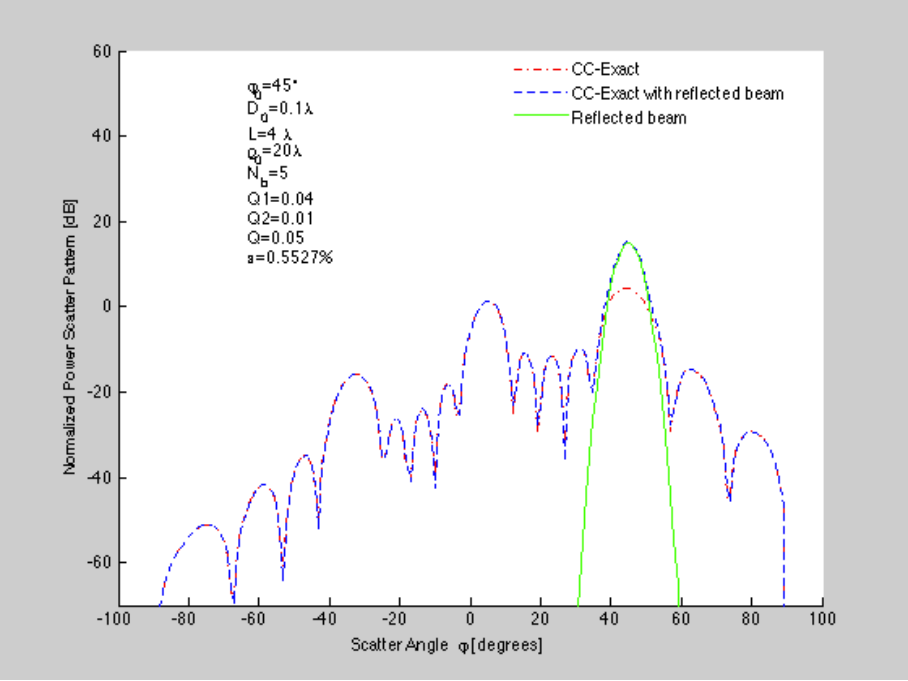

Figure 4.3b Normalized power scatter pattern versus scatter angle for the PEC scatter surface in Figure 4.1 of length $2L = 8\lambda$ and height $D_0 = 0.1\lambda$.

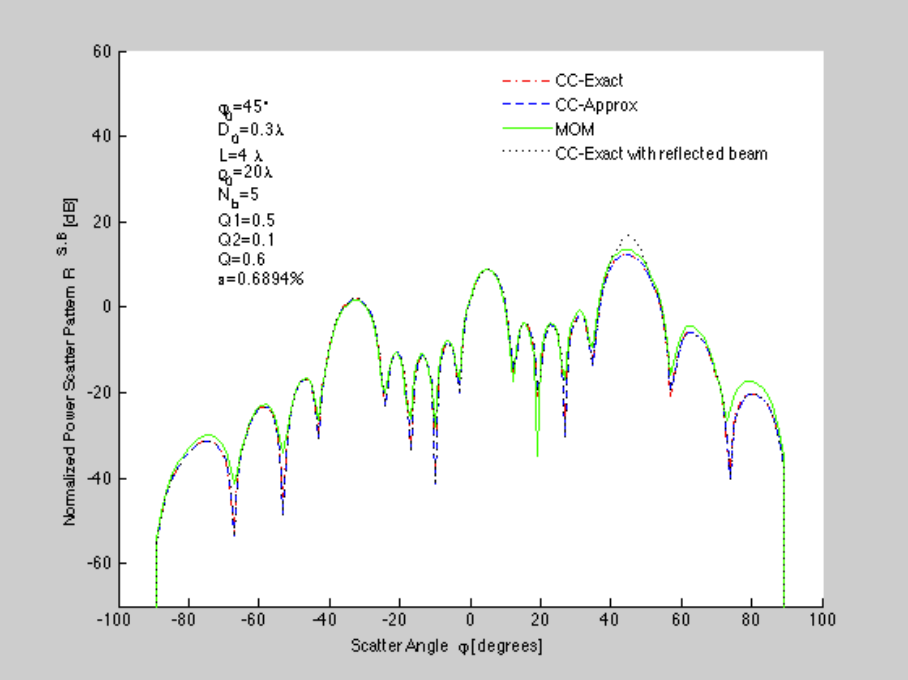

Figure 4.4a Normalized power scatter pattern versus scatter angle for the PEC scatter surface in Figure 4.1 of length $2L = 8\lambda$ and height $D_0 = 0.3\lambda$.

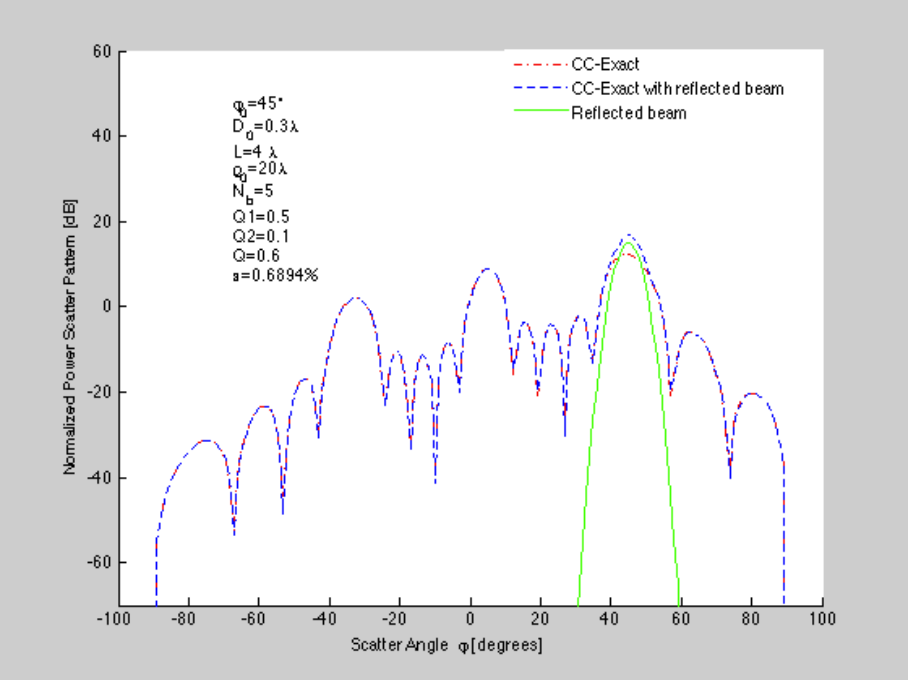

Figure 4.4b Normalized power scatter pattern versus scatter angle for the PEC scatter surface in Figure 4.1 of length $2L = 8\lambda$ and height $D_0 = 0.3\lambda$.

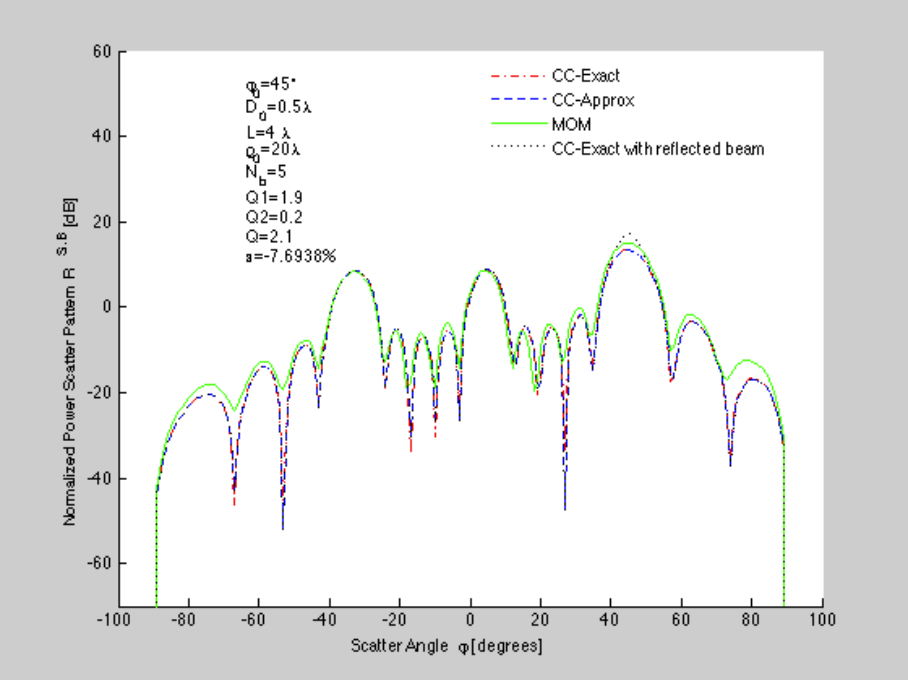

Figure 4.5a Normalized power scatter pattern versus scatter angle for the PEC scatter surface in Figure 4.1 with of length $2L = 8\lambda$ and height $D_0 = 0.5\lambda$.

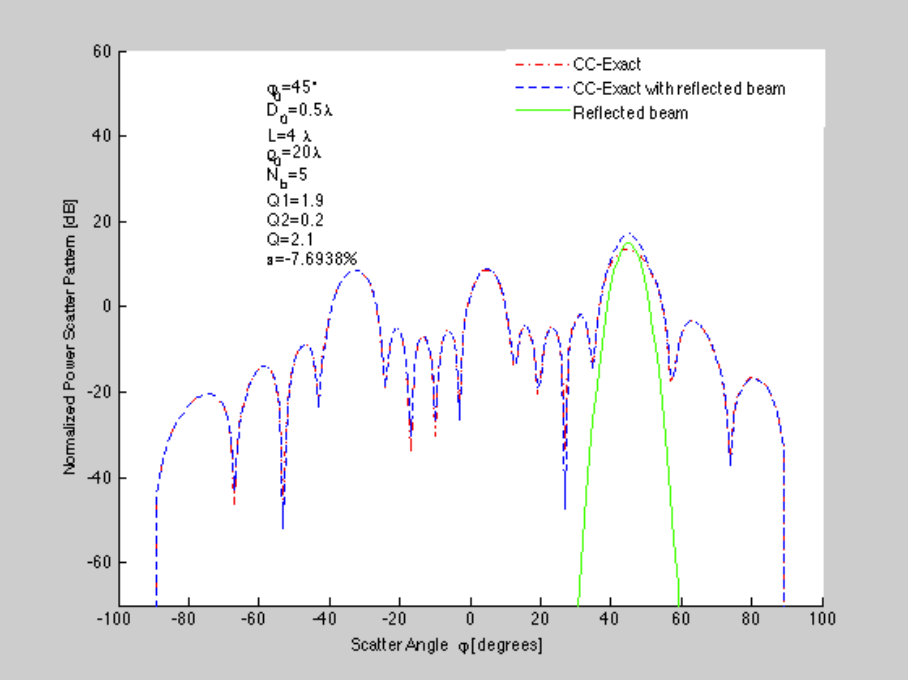

Figure 4.5b Normalized power scatter pattern versus scatter angle for the PEC scatter surface in Figure 4.1 of length $2L = 8\lambda$ and height $D_0 = 0.5\lambda$.

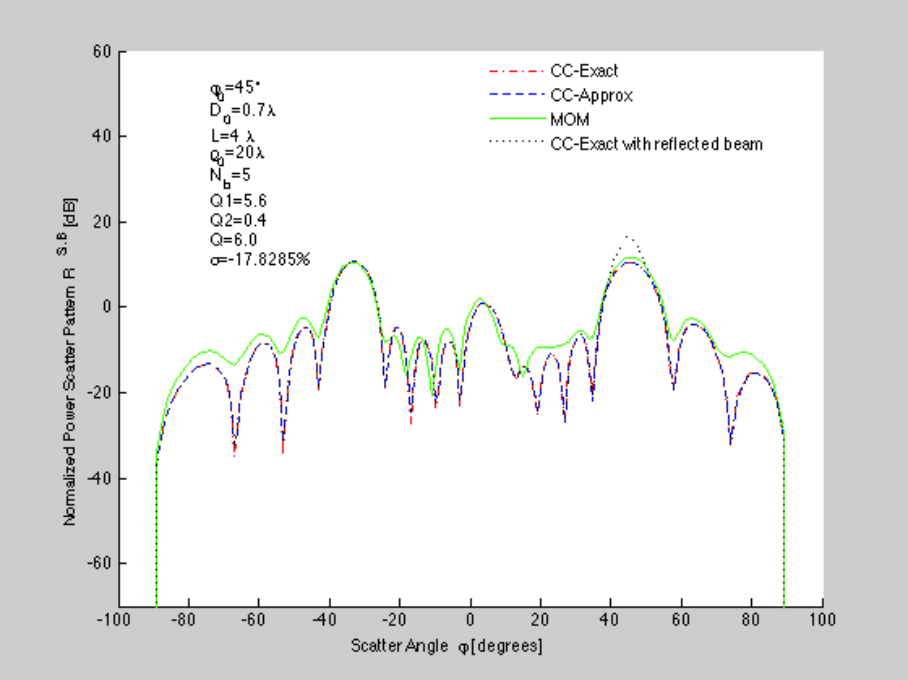

Figure 4.6a Normalized power scatter pattern versus scatter angle for the PEC scatter surface in Figure 4.1 of length $2L = 8\lambda$ and height $D_0 = 0.7\lambda$.

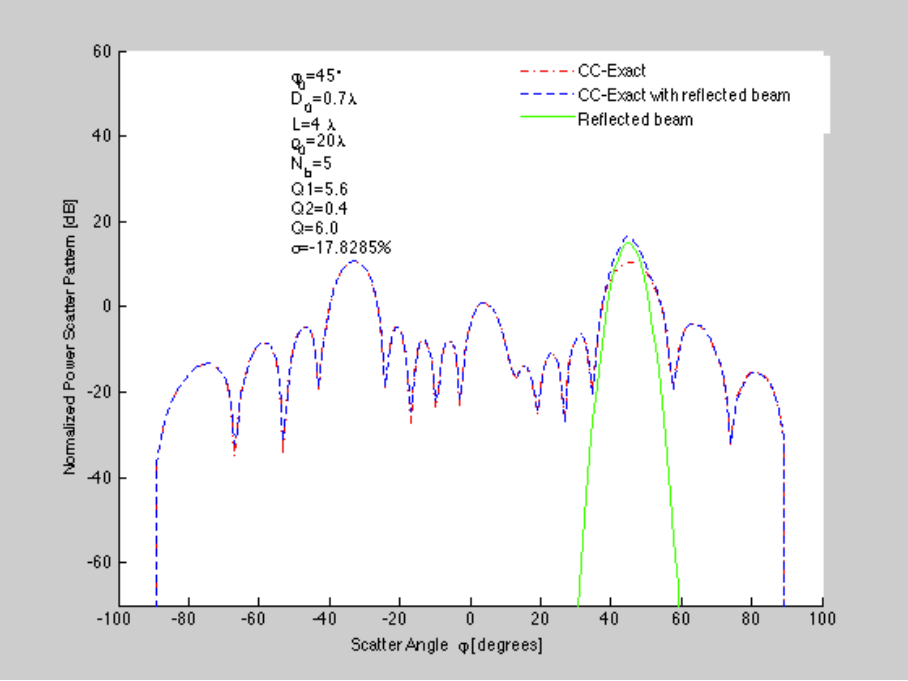

Figure 4.6b Normalized power scatter pattern versus scatter angle for the PEC scatter surface in Figure 4.1 of length $2L = 8\lambda$ and height $D_0 = 0.7\lambda$.

In Figures 4.7-4.15, three curves are drawn which give the normalized power scatter pattern of the CC-Exact and CC-Approx formulas and the MOM solution with fixed $Q = Q_1 + Q_2 = 0.6 + 0.1 = 0.7$ because of the fixed parameters of the scattering surface. Comparison of the results in Figures 4.7-4.15 show excellent agreement. In addition, the Q values and the power criterion ε are shown to be small, which indicates that the CC method is accurate.

Comparisons of Figures 4.7 to 4.10 show that larger incident waist size w_0 produces narrower scattered lobes. A larger waist size means the higher collimated beams results.

Comparisons of Figures 4.11 to 4.15 show that as the distance from the antenna and the scatter surface increases, the scattered pattern develops many additional scatter lobes in different directions. As ρ_0 increases, the incident beam broadens which allows more of the rough scatter surface to affect the scattering and results in the pattern getting rougher and less focused, which is similar to plane wave scattering.

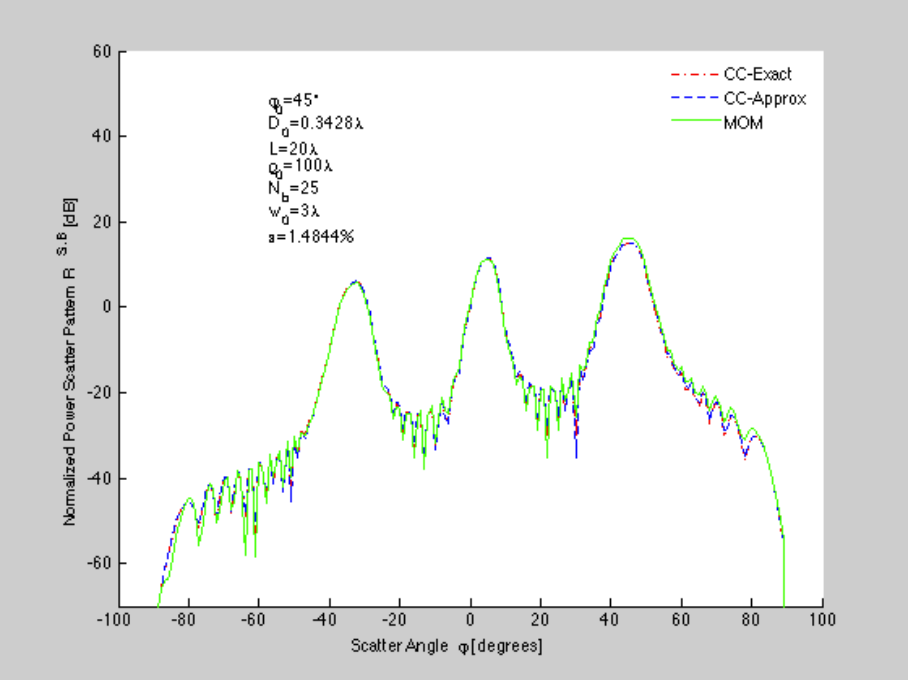

Figure 4.7 Normalized power scatter pattern versus scatter angle for the PEC scatter surface with 25 bumps, height $D_0 = 0.3428\lambda$, length $2L = 40\lambda$, distance $\rho_0 = 100\lambda$ and beam waist $w_0 = 3\lambda$.

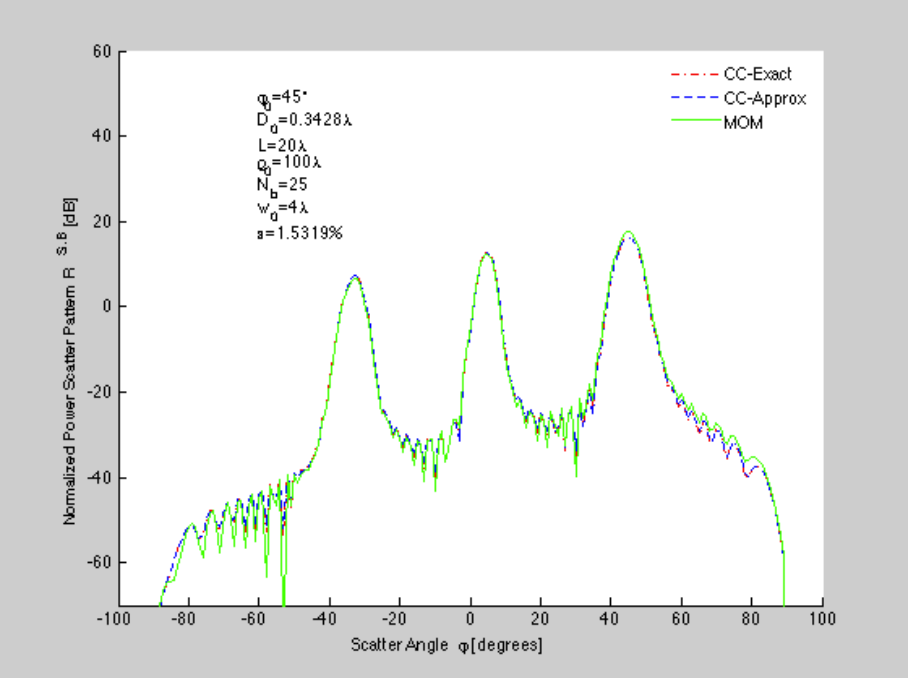

Figure 4.8 Normalized power scatter pattern versus scatter angle for the PEC scatter surface with 25 bumps, height $D_0 = 0.3428\lambda$, length $2L = 40\lambda$, distance $\rho_0 = 100\lambda$ and beam waist $w_0 = 4\lambda$.

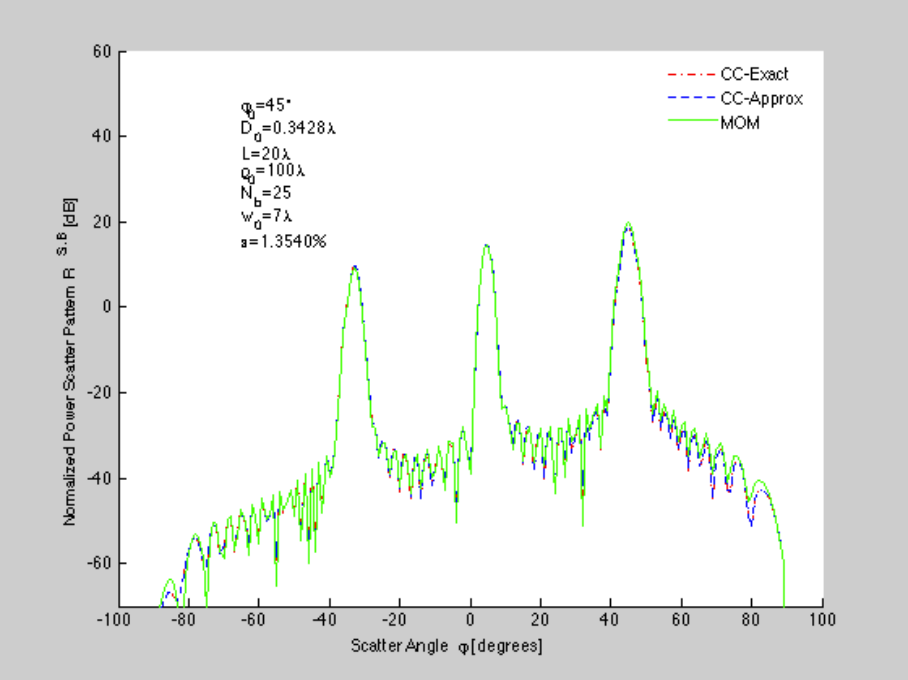

Figure 4.9 Normalized power scatter pattern versus scatter angle for the PEC scatter surface with 25 bumps, height $D_0 = 0.3428\lambda$, length $2L = 40\lambda$, distance $\rho_0 = 100\lambda$ and beam waist $w_0 = 7\lambda$.

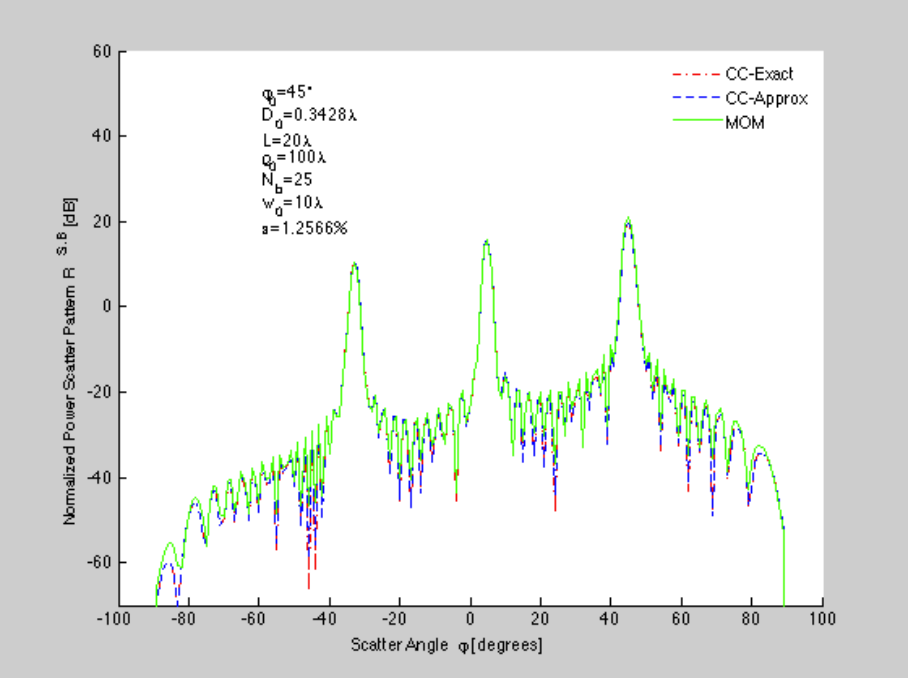

Figure 4.10 Normalized power scatter pattern versus scatter angle for the PEC scatter surface with 25 bumps, height $D_0 = 0.3428\lambda$, length $2L = 40\lambda$, distance $\rho_0 = 100\lambda$ and beam waist $w_0 = 10\lambda$.

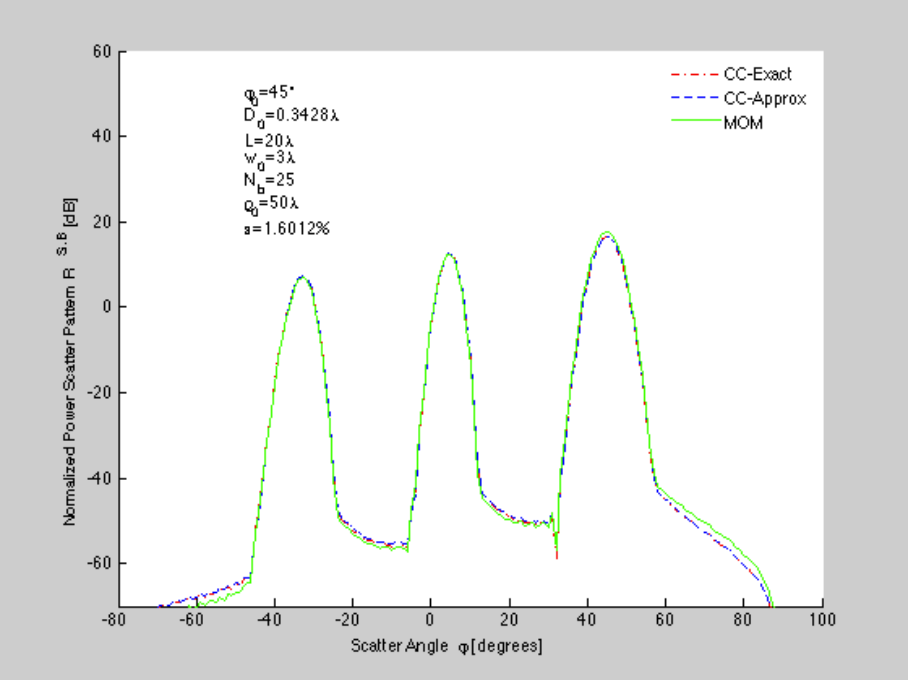

Figure 4.11 Normalized power scatter pattern versus scatter angle for the PEC scatter surface with 25 bumps, height $D_0 = 0.3428\lambda$, length $2L = 40\lambda$, beam waist $w_0 = 4\lambda$ and distance $\rho_0 = 50\lambda$.

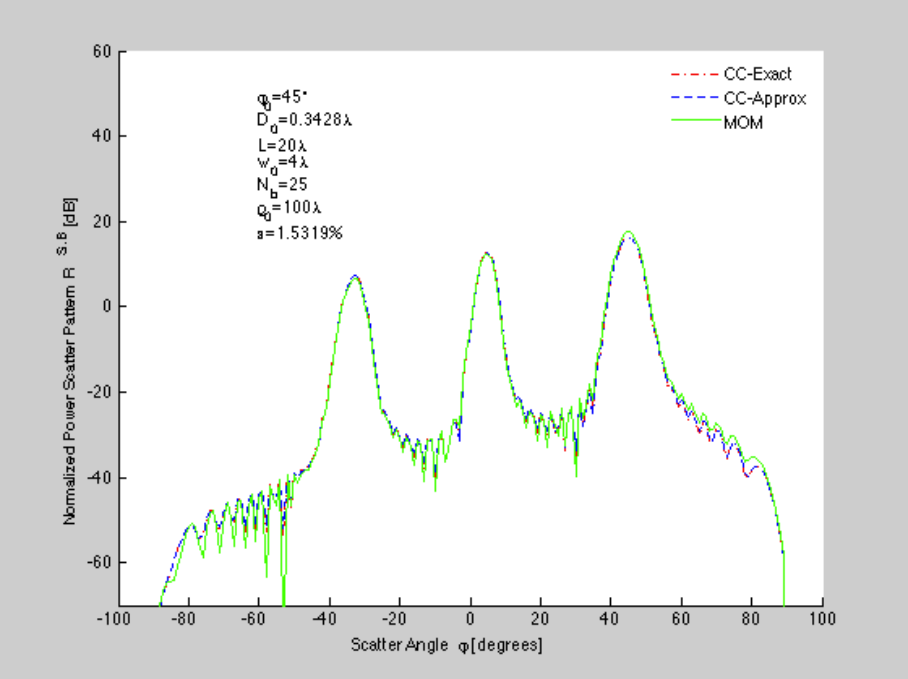

Figure 4.12 Normalized power scatter pattern versus scatter angle for the PEC scatter surface with 25 bumps, height $D_0 = 0.3428\lambda$, length $2L = 40\lambda$, beam waist $w_0 = 4\lambda$ and distance $\rho_0 = 100\lambda$.

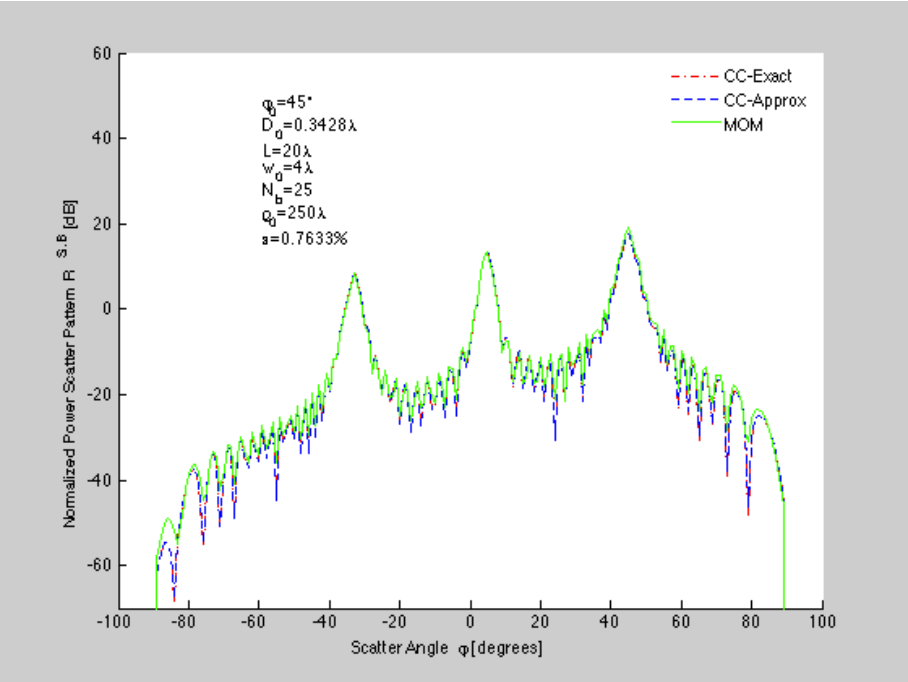

Figure 4.13 Normalized power scatter pattern versus scatter angle for the PEC scatter surface with 25 bumps, height $D_0 = 0.3428\lambda$, length $2L = 40\lambda$, beam waist $w_0 = 4\lambda$ and distance $\rho_0 = 250\lambda$.

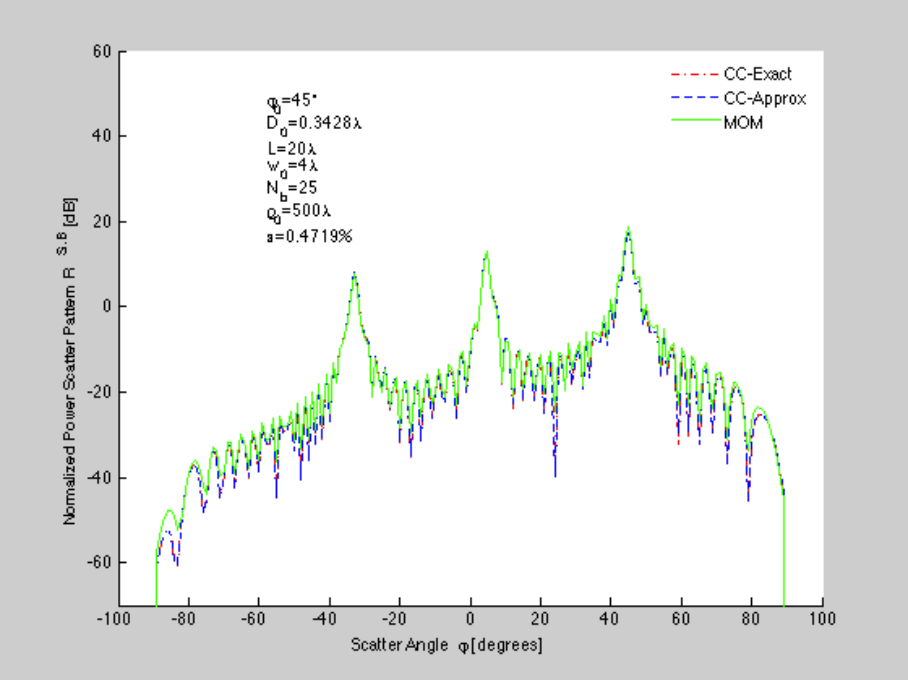

Figure 4.14 Normalized power scatter pattern versus scatter angle for the PEC scatter surface with 25 bumps, height $D_0 = 0.3428\lambda$, length $2L = 40\lambda$, beam waist $w_0 = 4\lambda$ and distance $\rho_0 = 500\lambda$.

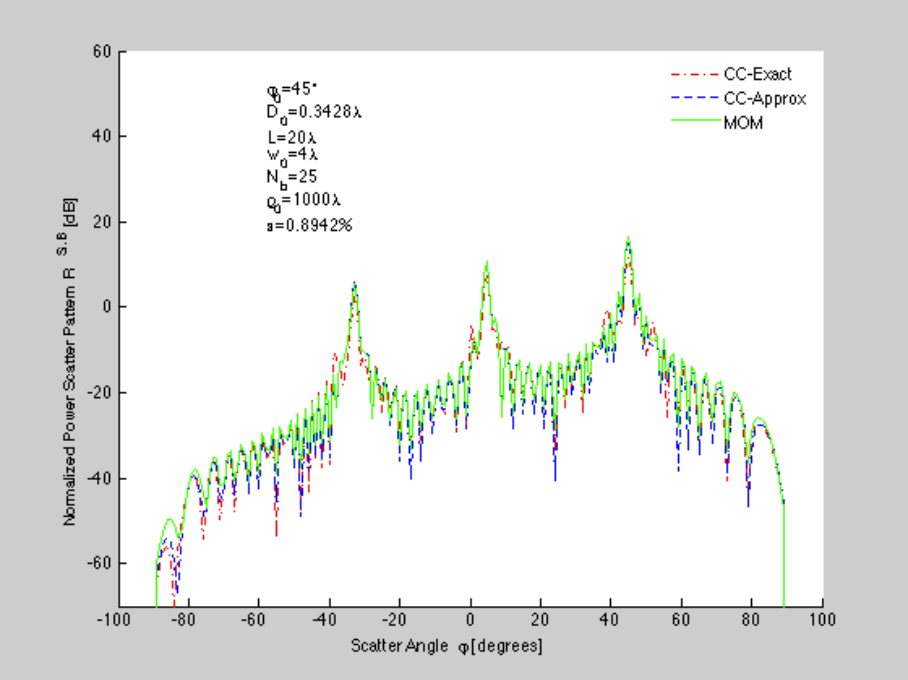

Figure 4.15 Normalized power scatter pattern versus scatter angle for the PEC scatter surface with 25 bumps, height $D_0 = 0.3428\lambda$, length $2L = 40\lambda$, beam waist $w_0 = 4\lambda$ and distance $\rho_0 = 1000\lambda$.

CHAPTER 5

CONCLUSIONS AND SUGGESTIONS

A full–wave theory of beam wave scattering from deterministic rough surfaces called the Correction Current (CC) method was presented. The method was applied to the two-dimensional scatter problem with a deterministic one dimensional scatter surface profile. The CC method involves a primary field and radiation modes, which do not satisfy Maxwell's source-free equations, but do satisfy Maxwell's equations with distributed current sources. The scatter problem is solved by eliminating these distributed current densities in an iterative procedure which produces a composite field that satisfies all requirements, but eliminates the current distributions by mutual compensation. The first-order solution of the CC method for beam wave scattering was shown to be accurate over a wide range of surface parameters. Comparisons were made between the CC-method and MOM method which showed very good agreement.

The present thesis has addressed the TE-polarization case of beam scattering from a deterministic rough scatter surface. Suggestions for further studies include that of the TM-polarization case and beam wave scattering by more general random rough surfaces.

REFERENCES

[1] Schwering F. K., Whitman G. M. & Triilo A. A. (2004). New full-wave theory for scattering from rough metal surfaces- The correction current method: The TE-polarization case. *Waves Random Media, 14*, 23-60.

[2] Whitman, G. M., Yoon, B. T., & Schwering, F. K. (2008). New Full Wave Theory for Plane Wave Scattering From Rough Dielectric Surfaces- The Correction Current Method: TE Polarization. *IEEE Transactions on Antennas and Propagation, 56*, 2002-2017.

[3] Saleh, Bahaa E. A. & Teich M. C. (2004). Fundamentals of Photonics. New York: John Wiley & Sons. Chapter 3, "Beam Optics", 80-107.

[4] Collin, R. E. (1994). Scattering of an incident Gaussian beam by a perfectly conducting rough surface. *IEEE Transactions on Antennas and Propagation, 42*, 70-74.

[5] Balanis C. A. (2012). Advanced Engineering Electromagnetic. New York: John Wiley & Sons. Chapter 11, "Scattering", 583-589.